### Deciphering the Fracture Initiation Mechanism in Additive Manufactured 17-4 Steel

Anik Das Anto<sup>1</sup>, Surajit Dey<sup>2</sup> and Ravi Kiran<sup>3</sup>

1

2

Abstract: Additive manufacturing (AM) provides exceptional geometrical freedom to the 3 4 architects and designers and enables the construction of architecturally exposed steel structures. 5 However, the AM structural elements inherently possess microscale defects that can affect their 6 ductility. This study aims to identify the fracture-initiating mechanism in AM 17-4 stainless steel 7 that is popularly used owing to its excellent engineering properties. To this end, axisymmetric 8 cylindrical notched and un-notched tension specimens are manufactured employing Direct Metal 9 Laser Sintering (DMLS) from 17-4 stainless steel powder with established processing and build parameters. The test specimens were manufactured using a 90° build orientation with the build 10 plate and a layer thickness of 40 µm. Post-processing heat treatment was avoided as the study 11 focused on understanding the failure mechanism in as-built AM test specimens. Detailed 12 13 metallurgical analysis is performed employing scanning electron microscopy (SEM) and electron 14 backscatter diffraction. Subsequently, micro-Computed Tomography (CT) studies are conducted on the tension specimens before and after mechanical testing. Although the SEM analyses of 15 fracture surfaces are inconclusive, the micro-CT analysis revealed evidence of nucleation of new 16 microvoids, growth of existing voids, and void coalescence in the vicinity of the fracture surface, 17 which is unequivocal evidence for ductile fracture. Furthermore, the larger AM defects were found 18 19 to play an important role in lowering the ductility in addition to stress concentration, and the

<sup>&</sup>lt;sup>1</sup> Graduate Research Assistant, Department of Mechanical, Aerospace & Biomedical Engineering, The University of Tennessee Knoxville, Knoxville, TN 37996, email: <a href="mailto:aanto@vols.utk.edu">aanto@vols.utk.edu</a>

<sup>&</sup>lt;sup>2</sup> Graduate Research Assistant, School of Sustainable Engineering and Built Environment, Arizona State University, Tempe, AZ-85281, email: sdey34@asu.edu

<sup>&</sup>lt;sup>3</sup> Associate Professor (Corresponding author), School of Sustainable Engineering and Built Environment, Arizona State University, Tempe, AZ-85281, email: <a href="mailto:ravi.kiran@asu.edu">ravi.kiran@asu.edu</a>

- fracture was initiated when the AM defects coalesced over a length of around 600 µm. The conclusions of this study emphasize the importance of controlling the maximum size of defects in AM structural elements to improve their performance.
- **Keywords**: Ductile fracture; Microvoids; Micro-CT; EBSD analysis; and Metallurgical texture

#### Introduction

Additive manufacturing (AM) is used to fabricate three-dimensional objects layer-by-layer from powder, wire, or sheets using a computer-aided design (CAD) model (Frazier 2014). The main advantage of AM over the conventional subtractive fabrication and casting process is that it can quickly produce complex structural elements with optimized geometry and functionality in relatively small production units (Bajaj et al. 2020; He et al. 2020). Due to the convenience and geometric freedom in manufacturing complex components, AM has made significant strides in manufacturing prototypes and industrial components made of thermoplastic (Mattey et al. 2023), adhesives (Khosravani et al. 2021), polymers (Jasiuk et al. 2018), metals (DebRoy et al. 2018), and others. The present study focuses on understanding the fracture mechanism in metal AM.

Metal AM has made significant developments in various engineering fields such as aerospace (Blakey-Milner et al. 2021), automobile (Vasco 2021), healthcare (Rezvani Ghomi et al. 2021), and marine (Calle et al. 2020) among many others. The major benefits of AM which led to widespread adoption, include greater design and manufacturing efficiency (Buchanan and Gardner 2019), geometric freedom leading to free-form geometries, and reduced energy consumption due to the elimination of several fabrication activities such as drilling holes, sectioning members, etc. (Kanyilmaz et al. 2022). A recent report from the World Steel Association revealed that 52% percent of the global steel consumption is related to construction in the form of steel rebars, plates, and structural members (Kanyilmaz et al. 2022). Despite being the

top steel consumer, the construction sector has long been lagging in the adoption of AM technology where construction projects predominantly use traditional methods and working practices (Buchanan and Gardner 2019; Wu et al. 2016). Recently, metal AM has gained some traction in the construction industry where structural sections, connections, and pedestrian bridges have been manufactured using 3D printing technology (Gardner 2023). The AM parts manufactured for construction are larger in size compared to those used in other industries. This key difference in geometry leads to difficulty in post-processing heat treatment which is an important step in metal AM. Post-processing heat treatment is often used in metal AM to reduce internal residual stresses and inherent porosity, improve mechanical performance, and reduce anisotropy resulting from AM (Buchanan and Gardner 2019; Kanyilmaz et al. 2022). However, the large geometry of construction AM parts renders post-processing heat treatment unviable (Kanyilmaz et al. 2022). This motivated the present study in investigating the fracture behavior of as-built additively manufactured metal components.

Additive manufacturing of metal requires a heat source to melt the metal powder to provide the shape of the CAD model. The localized heating and rapid cooling with powdered feedstock act as a favorable environment for forming small cracks, unmelted particles, gas bubbles, and a lack of fusion during manufacturing (Sanaei et al. 2019). More specifically, defects from the fabrication processing stages are mainly responsible for the early fracture and failure in AM metals (Dennies 2021). Supply of optimized heat energy to the melt pool is necessary to melt the previously deposited layer and to ensure perfect bonding between layers. Without optimized process parameters such as laser power, layer thickness, hatch spacing, and scan speed can generate defects, including a lack of fusion (LOF) voids and keyhole pores (Mostafaei et al. 2022; Sanaei and Fatemi 2021; Singla et al. 2021). Lack of optimized energy supply to the melt pool may result

in inadequate melting, vaporization, poor bonding, and LOF defects. The defects in AM components can have sharp edges with an elongated shape located between the print layers (Gong et al. 2015; Xu et al. 2015). Moreover, excessive energy and low scanning speed to the melt pool will result in substantial vapor recoil forces and damaging convection currents, leading to spherical voids and gas bubbles due to the surface tension of the melt pool (King et al. 2015). It is challenging to remove gas pores by post-processing and depends on the solubility of the contaminated gas (Shao et al. 2017). At the time of re-melting during the deposition of the next layer, the gas bubble formed on top of the melt pool escapes to the gas bubble deeper in the melt pool, which generates keyholes that are a more detrimental form of porosity (Dilip et al. 2017). Overall, the defects in the AM metals can be minimized but impossible to eliminate. A proper statistical understanding of the defects and their spatial distribution can provide insights into the performance of the AM metallic components.

Defects in as-built AM steel may lead to early fracture due to reduced strength and ductility (Meng et al. 2021; Wilson-Heid et al. 2019). The fracture-initiating mechanism in the as-built AM 17-4 stainless steel is still elusive to the additive manufacturing community. There is also a lack of research in identifying the influence of AM defects on fracture initiation in as-built AM 17-4 stainless steel. Therefore, to understand the influence of AM defects on fracture, we need to quantitatively characterize the defect distribution in the as-built AM steel test specimens before and after a fracture. Furthermore, the effect of geometrical complexities or intricacies on AM defects remains unexplored, and their influence on fracture initiation is yet to be investigated.

The conventional practice of fractography includes optical microscopy and scanning electron microscopy (SEM) techniques. The extracted micrographs of the fracture surface of the test specimens are inspected for certain features to understand the fracture mechanism of the metal.

For example, the existence of river-like patterns and cleavage on the fracture surface indicates brittle fracture whereas, coalesced microvoid colonies indicate ductile fracture of the metal. However, the micrographs only provide information about specific sections of the sample that do not represent the whole part's structure with non-homogeneously distributed defects. Furthermore, the fracture surface may consist of features pertaining to different fracture types and the conventional fractography techniques might fail to identify the predominant fracture mechanism in the metal. In these cases, a non-destructive technique such as micro-computed tomography (micro-CT) is more appropriate for investigating the fracture mechanism in the internal structure of the test specimens and controlling the quality of the additively manufactured metals (Elmoutaouakkil et al. 2002). The present study investigates the fracture evolution in the whole specimen using micro-CT instead of focusing only on the fracture surface or any other crosssection which is the usual practice in conventional stop-cut-see experiments. Furthermore, the inherent pores present in the AM components induced by the additive manufacturing process may initiate early fracture in the specimens (Berez et al. 2022; Wilson-Heid et al. 2019). The current study aims to investigate the influence of AM-induced defects on the deformation behavior and fracture-initiating mechanism in the as-printed AM 17-4 stainless steel specimens using SEM and micro-CT analysis. The objectives of this are as follows: 1) to quantify the growth of the number of voids and void volume in AM specimens after deformation, 2) to determine the statistical distribution of void features of AM steels before and after deformation, 3) to investigate the influence of sudden geometrical changes on the size and density of AM defects and 4) to elucidate the fracture initiating mechanism and evaluate the characteristic length over which the voids must grow to initiate fracture for AM 17-4 stainless steel.

# 2. Materials and Methods

89

90

91

92

93

94

95

96

97

98

99

100

101

102

103

104

105

106

107

108

109

110

111

# 2.1 Additive Manufacturing Process Parameters and 17-4 Steels

The specimens used in the present study were additively manufactured employing Direct Metal Laser Sintering (DMLS) from 17-4 stainless steel spherical powder with a particle diameter of 36-44 µm. 17-4 stainless steel specimens were printed using the following process parameters: laser power of 220 W, 70 µm laser beam diameter, scanning speed of 755 mm/s, and a 0.11mm hatching space. A 90° build orientation with the build plate and a layer thickness of 40 µm are used as build parameters. Since the present study focuses on understanding the deformation behavior and failure-initiating mechanism in the as-printed AM steel specimens, post-processing heat treatment was avoided for the test specimens which is typically employed to reduce the material defects in AM specimens.

17-4 stainless steel was used in the present study due to its wide range of engineering applications. 17-4 stainless steel finds its application in aerospace (Singh et al. 2022), surgical instrumentation (Gonzalez-Nino et al. 2021a; Soja et al. 2020), naval (Huang et al. 2022), nuclear (Bai et al. 2021), structural systems (Gonzalez-Nino et al. 2021b), and petrochemical industries (Jiang et al. 2020) due to its high strength, fracture toughness, hardness, and excellent corrosion resistance (Bai et al. 2021; Huang et al. 2022; Jiang et al. 2020; Singh et al. 2022; Soja et al. 2020). The material properties of 17-4 stainless steel can be partly attributed to the chemical composition of the steel powder, which is presented in Table 1. 17-4 stainless steel powder comprises 15-17.5 wt.% chromium, 3-5 wt.% nickel, and 3-5 wt.% copper which combinedly provide high corrosive resistance and conductivity (Avner 1974; Ye et al. 2012). The microstructure of 17-4 stainless steel was studied in the laboratory using small disc-shaped specimens which were ground using silicon carbide (SiC) paper with grit size in the following order: 60, 120, 400, 800, and 1200. Furthermore, the ground steel specimens were polished using alumina suspension and were subsequently etched

using Fry's reagent. Finally, the etched steel specimens were observed under a light microscope.

The melt pool boundaries, layer thickness, and hatch spacing are clearly visible in the optical micrograph (see

Figure 1). Moreover, the microstructure governs the mechanical properties, and hence, the microstructural characterization process used in this study is discussed in the following section.

#### 2.2 Microstructure Characterization

135

136

137

138

139

140

141

142

143

144

145

146

147

148

149

150

151

152

153

154

155

156

157

The fracture initiation mechanism for rolled 17-4 steel has been studied (Alnajjar et al. 2020; Suri et al. 2006; Wu and Lin 2002). The wrought 17-4 steel microstructure contains a martensitic structure, whereas the AM 17-4 steel is  $\delta$ -ferritic with elongated columnar grains along the build direction (Alnajjar et al. 2020). The presence of different phases can be confirmed by their texture in micrographs but is difficult to identify automatically when there exists an overlap between phases (Naik et al. 2019). This quantified the microstructure of AM 17-4 steel by employing Electron Backscatter Diffraction (EBSD). EBSD is a scanning SEM-based technique with a diffractor that reveals crystallographic details such as phase, texture or crystallographic orientations, grain size, grain shape, and average grain orientation (Zaefferer et al. 2012). The samples of EBSD analysis must be prepared by carrying out several steps: sectioning, grinding, polishing, and etching using the standard EBSD sample preparation technique (Sun et al. 2018). The samples were mounted in 1-inch epoxy rounds. These were then ground on SiC papers, starting at 240 grit and then using 320, 400, 600, and 1200 grit at 200 rpm. After this, the samples were diamond polished for 10 minutes each on 6 μm, 3 μm, and 1 μm. Final polishing using 50nm colloidal silica polish was performed for 30 minutes. Once polished, the samples were coated with 5nm of carbon to maintain conductivity in the SEM. EBSD analysis was performed using JEOL 6500 SEM integrated with an EBSD system to investigate the grain morphology and crystallographic orientations. The following settings were maintained for the EBSD investigation: 20 nA of beam current, 20 kV of accelerating voltage, 70° specimen tilt angle, 78.66% hit rate, and an acquisition speed of 1399.76 Hz. The band contrast microstructure of the 17-4 AM stainless steel, analyzed using the SEM, is illustrated in

Figure 2. The grain size of AM steel is larger than that of wrought steel, and the grain structure of AM steel is not as equiaxed as wrought steel. The martensitic structure can provide maximum hardness, and the ferritic structure is soft and ductile (Sajid et al. 2020). So, crack initiation and growth are easier in ferritic AM steel than in martensitic wrought steel (Alnajjar et al. 2020). EBSD orientation maps and FCC/BCC phases for the horizontal and vertical cross-sections are shown in

Figure 3. There is a significant difference in grain orientation and grain size of the horizontal and vertical sections of the AM 17-4 stainless steel test specimens. The average length of the grains in the horizontal and vertical cross-sections are  $3.38~\mu m$  and  $4.07~\mu m$ , respectively. Equiaxed and columnar grains were identified in both the horizontal and vertical sections, as shown in

Figure 2. The horizontal section of the test specimen is dominated by equiaxed grains, whereas elongated columnar grains are primarily identified in the molten pool boundaries of the vertical section. The maximum aspect ratio ranges from 1.06 to 8.12 and 1.06 to 15.03 for the horizontal and vertical sections, respectively. The EBSD analysis also indicates that the 17-4 stainless microstructure is largely dominated by the BCC/BCT phases compared to that of the FCC phase, which is consistent with the literature (Alnajjar et al. 2020; Sun et al. 2018). The presence of the ferritic phase in the AM 17-4 stainless steel could provide high ductility, but inherent defects

in the as-built AM components lead to early failure. Thus, a comprehensive study of the fracture initiation mechanism is presented in the following sections.

# 3. Experimental and Simulation Details

#### 3.1 Geometry of the Specimens and FE Analysis

In this study, one reference unnotched (RU) and C-notched (CN) axisymmetric cylindrical specimens were considered. Three different notch radii (CN1: 0.5 mm, CN2: 1 mm, and CN3: 1.5 mm) were used to achieve a wide range of stress triaxialities and to understand the response of the material when subjected to a sudden change in geometry in the critical section (Sajid and Kiran 2018). Furthermore, these specimens were also used to study the AM defects near geometrical discontinuities. The geometric details and dimensions of the AM 17-4 stainless steel specimens are provided in

Figure 4. Figure 5 presents the images of the AM 17-4 test specimens subjected to uniaxial tension test in the present study. Uniaxial tension tests were performed using a servo-hydraulic MTS 809 load frame. A uniform displacement rate of 0.02mm/s was maintained during the uniaxial tension tests. The elongation of the deformed test specimens was monitored using a contact extensometer with a 1-inch (25.4 mm) gauge length (Epsilon model 3542). The engineering stress-strain load curves obtained for various test specimens are shown in

Figure 5. Additively manufactured 17-4 test specimens subjected to uniaxial tensions tests

199 Figure 6.

Finite element analysis (FEA) was conducted using the commercially available FEA package ABAQUS® for both unnotched and notched test specimens. The finite element models were discretized using four-node bilinear axisymmetric CAX4 elements available in the ABAQUS® library. Owing to the axisymmetric geometry of the cylindrical test specimens, a quarter of the test specimens were modeled using FEA resulting in reduced computation cost. Furthermore, the critical stresses and strains were observed near the notched section of the test specimens subjected to uniaxial tension tests. To capture the critical stress and strain gradient near the notches, a finer mesh size of 0.025 mm was maintained near the notched section of the test specimens. A comparatively coarser mesh was used in the regions away from the notched section to reduce computation costs. Figure 7 presents the typical finite element mesh used for the unnotched and notched test specimens. J<sub>2</sub> plasticity constitutive model was used to capture the material non-linearity, and a non-linear geometric solver was used to obtain the finite element solutions. The strain hardening curve for the J<sub>2</sub> plasticity model was obtained from the experimental stress-strain curve of the reference unnotched specimen and the Ramberg-Osgood relationship (see

Figure 8a). The engineering stress-strain curve obtained from FEA was compared with the experimental stress-strain curve to validate the finite element model (see

Figure 8b). The stress triaxiality and equivalent plastic strain distributions across the critical section (least cross-section) of the test specimens at fracture were extracted from the non-linear finite element analysis and are presented in

### Figure 9 and

200

201

202

203

204

205

206

207

208

209

210

211

212

213

214

215

216

217

218

219

220

221

222

Figure 10, respectively. The maximum stress triaxiality across the critical cross-section of the steel specimens at fracture ranged from 0.3 to 1.13. Equivalent plastic strains have higher

values in the vicinity of the notches in the notched specimens. Higher stress triaxiality is found to decrease the fracture strains in metals (Sajid and Kiran 2018).

# 3.2 Investigation of Fracture Type Employing SEM

SEM analysis of the fracture surfaces of the AM 17-4 stainless steel test specimens was conducted to decipher the microscopic damage mechanism. The fractured samples were attached to cylindrical aluminum mounts with double-sided XYZ adhesive tape to view the fracture surface of the test specimens. The images of the fracture surfaces were obtained at an accelerating voltage of 15kV using a JEOL JSM-6490LV SEM (JEOL USA, Peabody MA, USA). Typical SEM micrographs of the fracture surfaces of the reference unnotched (RU) and notched (CN1) test specimens are presented in

## Figure 11 and

Figure 12, respectively. Furthermore, magnified images of five different locations on the fracture surface of the test specimens are also presented. The regions were divided based on varying stress and strain states across the cross-section of the test specimens, which was obtained using the finite element analysis discussed earlier (see

#### Figure 9 and

Figure 10). Fractures in steel can be classified into three categories: ductile fracture, intergranular fracture, and transgranular cleavage fracture. Ductile fracture in the steel originates from microvoid nucleation followed by growth of the voids and finally coalescence leading to fracture during plastic deformation (Kiran and Khandelwal 2013, 2014a; Kuwamura and Yamamoto 1997). The microvoids nucleate due to debonding and/or cracking of the secondary particles in the steel matrix. These nucleated microvoids and/or existing material defects elongate and dilate due to the

applied external load on the test specimen. Finally, these microvoids and/or defects coalesce over a critical length to form cracks that initiate ductile fracture in the steel specimens (Kanvinde and Deierlein 2006; Kiran and Khandelwal 2014b; Wen and Mahmoud 2016; Ziccarelli et al. 2023). Transgranular fracture is a brittle cleavage fracture characterized by river-like patterns and is caused due to the propagation of cracks through the grain interiors (Naik and Kiran 2019; Pineau et al. 2016). The SEM micrographs of the test specimens presented in

Figure 11 and

Figure 12 show the majority of dimples with traces of river-like patterns on the fracture surface. Although small dimples with an average equivalent spherical diameter of  $\sim 1~\mu m$  are visible on the SEM fractographs, it is challenging to identify coalesced microvoid colonies on the fractographs of the test specimens responsible for ductile fracture in steel. The dimples' sizes are more prominent in SEM fractographs of conventional 17-4 PH steel compared to AM specimens, and the coalesced void colonies can be identified on the fracture surfaces (see

Figure 13), similar study has been done for 17-4 PH conventional steel (Dey, Surajit et al. n.d.). Therefore, the SEM study of fractographs of the AM 17-4 stainless steel specimens is insufficient in identifying the fracture initiation mechanism in the fractured steel specimens. Thus, a three-dimensional void quantification technique needs to be adopted to elucidate the fracture initiation mechanism in AM 17-4 stainless steel specimens.

# 3.3 Defect Quantification Employing Micro-CT

The internal manufacturing defects in the AM steel specimens are difficult to detect using surface identification techniques. The defects in the as-built steel specimens considered in the present study will be discussed in detail later in the section. Three-dimensional (3D) non-

destructive techniques, namely, Archimedes method and gas pycnometry may be used to quantify the volume of internal defects in the test specimens; however, these methods are incapable of providing quantitative characteristics of the internal defects in the specimens (Wits et al. 2016). Micro-CT is a 3D non-destructive technique initially developed for medical applications. Micro-CT is equipped with X-ray beams and detectors that extract images of a 3D object about an axis of rotation and reconstruct a 3D model of the object (Sanaei et al. 2019). In civil engineering, Micro-CT has been extensively used in studying granular materials (Borela et al. 2021; Roy et al. 2022; Wang et al. 2004; Wang and Frost 2012). Recently, Micro-CT has been introduced to AM metals for in-situ measurement of part geometry and defect characterization (Sanaei et al. 2019; Wits et al. 2016). In the present study, micro-CT is used to characterize the manufacturing defects in the as-built AM steel test specimens, and the defect characteristics were utilized to understand the fracture-initiating mechanism in the as-built steel specimens.

The micro-CT scans were conducted using GE Phoenix v|tome|x s X-ray computed tomography system equipped with a 180 kV nano focus X-ray tube and a high-contrast GE DXR250RT flat panel detector (GE Sensing & Inspection Technologies GmbH) at a voltage of 150 kV and a current of 350 μA with a diamond target. Detector timing ranged from 333-500 milliseconds, and 600-1000 projections were acquired. A voxel resolution of 16.9 μm was achieved during the scanning with a sample magnification of 11.835X. The acquired images were reconstructed into a volume data set using GE datos|x 3D computer tomography software version 2.8.0 RTM (GE Sensing & Inspection Technologies GmbH). A minimum of 8 voxels were considered a threshold for a single void to remove reconstruction artifacts and noise, resulting in a void volume of 38,608.4 μm<sup>3</sup> and an equivalent spherical diameter of 41.93 μm. The minimum detectable void in the micro-CT scan is close to the layer thickness (40 μm) in the DMLS technique

and the mean diameter of the particles (around 40  $\mu$ m) used in additive manufacturing of the 17-4 stainless steel specimens. It will be possible to capture the common manufacturing defects in asbuilt AM components with this voxel resolution.

All the notched and unnotched AM 17-4 stainless steel specimens were subjected to micro-CT scans both before and after the fracture. The tensile test specimens were scanned over a distance of 15 mm from the center of the gauge length. The scanned section of each test specimen was further divided into three separate 5 mm zones: A, B, and C, for the evaluation of local characteristics of voids before and after deformation (see

Figure 14). The number of zones is limited to three, so a sufficient number of defects are available in each zone for statistical analysis of the defect characteristics. As shown in

Figure 14, zone A is located near the center of the gauge section of the test specimens. Zone B is adjacent to Zone A, whereas Zone C is adjacent to Zone B and is located farthest away from the critical section of the test specimen. Zone A is anticipated to experience the largest plastic deformation since it is closest to the critical section. In contrast, zones B and C are expected to undergo relatively less plastic deformation. Defect analysis was performed on the reconstructed 3D image of the steel test specimens using VGStudio Max version 2022.2 (Volume Graphics, Inc.). The features of defects include equivalent spherical diameter, sphericity, number of voids, and void volume fraction. Statistical analysis was conducted for the defect features in the following section.

### 4.0 Results and Discussion

#### 4.1 Growth of the Number of Voids and Void Volume Fraction after Deformation

The present study quantified the change in the number of voids and void volume fraction after deformation in the AM as-built 17-4 stainless steel test specimens. The average void count per cubic millimeter in the three zones (zones A, B, and C) for undeformed specimens RU, CN1, CN2, and CN3 were observed to be 185, 237, 310, and 362, respectively. After the fracture, the average void count per cubic millimeter increased to 299, 390, 794, and 887 in the three zones for specimens RU, CN1, CN2, and CN3, respectively. This implies that the number of voids per cubic millimeter increased by 61.62%, 64.56%, 156.13%, and 145.03% in the three zones after fracture for specimens RU, CN1, CN2, and CN3, respectively (see

Figure 15). The increase in the number of voids after fracture indicates void nucleation in the test specimens during the deformation process.

The void volume fraction is a measure of the volume of void per unit volume of material, which is a ratio of the volume of the defects to the total volume of the material in the individual specimen. The average void volume fraction in the three zones of the undeformed specimens RU, CN1, CN2, and CN3 was found to be 2.25%, 3.32%, 3.77%, and 4.19%, respectively. After the fracture, the average void volume fractions of the three zones increased to 3.67%, 5.01%, 6.00%, and 6.62% for specimens RU, CN1, CN2, and CN3, respectively. Therefore, the average void volume fractions in the three zones increased by 62.70%, 50.70%, 59.20%, and 57.86% after fracturing in specimens RU, CN1, CN2, and CN3, respectively (see

Figure 16). The increase in void volume fraction can be attributed to two phenomena, namely, void nucleation and void growth.

#### 4.2 Statistical Distribution of Void Features Before and After Deformation

Statistical analysis of the features of the voids in both undeformed and deformed conditions is presented in this section. Equivalent spherical diameter is a parameter for understanding the defect size present in the test specimens, which is the diameter of a sphere with an equal defect volume. The equivalent spherical defect diameter distribution for undeformed and deformed zones A, B, and C of the reference unnotched specimen RU are presented in

Figure 17. As evident from the defect equivalent spherical diameter probability density plots, the distributions are asymmetric, with the mean defect size being larger than the median, thereby resulting in positively skewed distributions (see Table 2). Based on the statistical analysis of the equivalent spherical defect diameter using a probability density plot, the defect sizes present in the notched and unnotched test specimens before and after fracture were observed to follow a lognormal distribution. A distribution is considered to be lognormal when the logarithm of the random variable is observed to follow the Gaussian distribution and is applicable for non-negative data. Previously, lognormal distribution was used to represent the pore size distribution in metallic and cementitious materials (Eliaz et al. 2020; Kim et al. 2012). The probability density function of a lognormal distribution is given as (Allen 1945; Limpert et al. 2001):

$$y = \frac{1}{x s^* \sqrt{2\pi}} exp\left(\frac{-(\ln x - \bar{x}^*)^2}{2s^{*2}}\right), \qquad 0 < x < \infty$$
 (1)

where, x is the equivalent spherical defect diameter.  $\bar{x}^*$  and  $s^*$  are two lognormal distribution parameters that denote the mean and standard deviation of the natural logarithm of equivalent spherical defect diameter, respectively.  $\bar{x}^*$  and  $s^*$  are given as

$$\bar{x}^* = \ln(\bar{x}), \quad s^* = \ln(s) \tag{2}$$

where,  $\bar{x}$  and s are the mean and standard deviation of the equivalent spherical diameter.

More than 98% of the defects present in the unnotched specimen RU and notched specimens CN1, CN2, and CN3 at both undeformed and deformed states were observed to have equivalent spherical defect diameters ranging between 40  $\mu$ m and 120  $\mu$ m. Furthermore, the mean ( $\bar{x}$ ) of the equivalent spherical defect diameter did not exhibit significant variation before and after fracture in all three zones for all the unnotched and notched specimens (see

351

352

353

354

355

356

357

358

359

360

361

362

363

364

365

366

367

368

369

370

371

372

373

Figure 17 and Table 2). The mean equivalent spherical diameter after fracture for all the zones was observed to be similar or slightly lesser than that observed before fracture. The slightly lesser mean equivalent spherical diameter can be attributed to the smaller new microvoids nucleated during the plastic deformation in the material. The standard deviation of the size distributions in the test specimens is approximately similar for all the zones after fracture. This implies that the microvoids grew uniformly across the different zones. Furthermore, the standard deviation of the void sizes remained approximately the same across the zones before and after fracture, implying that the majority of the microvoids in a particular zone evolved uniformly throughout the deformation process. However, the equivalent spherical diameter of the larger defects experienced a substantial change after the fracture (see Table 2). For the largest 500 voids in zone A of the undeformed specimens, the equivalent spherical diameter increased by 11.10%, 7.63%, 2.81%, and 3.11% for specimens RU, CN1, CN2, and CN3, respectively, after the fracture. The equivalent spherical diameter of the largest 200 defects in zone A of the undeformed specimens increased by 13.02%, 8.49%, 5.88%, and 8.77% for the specimens RU, CN1, CN2, and CN3, respectively, after the fracture. Therefore, the significant change in the size of the larger defects after fracture indicates that larger defects present in the undeformed specimens dictate the fracture initiation in AM steel. The median, 90th percentile, and 95th percentile equivalent spherical defect diameter in zone A of specimens RU, CN1, CN2, and CN3 for undeformed and deformed conditions are provided in Table 3. In CN1, CN2, and CN3 specimens, the median, 90th percentile, and 95th percentile of the equivalent spherical diameter of defects decreased. This can be attributed to higher microvoid nucleation in the notched specimens due to the high-stress triaxiality. However, the nucleated voids did not grow significantly due to low fracture strain. The median, 90th percentile, and 95th percentile equivalent spherical defect diameter increased in the RU specimen, which may be attributed to significant growth of the nucleated voids due to higher fracture strain compared to that of the notched specimens.

The sphericity distributions of the defects in zones A, B, and C before and after fracture for specimens RU are presented in

Figure 18. The value of sphericity is unity for perfectly spherical defects, whereas highly irregular defects have a sphericity close to zero. Based on statistical analysis using the probability density plot, the sphericity distributions of the defects present in zones A, B, and C of the unnotched test specimens before and after fracture were observed to follow the Gaussian distribution. Sphericity distribution maintains normal Gaussian distribution for all the test specimens where the mean and median are almost the same (see Table 4). The mean sphericity of defects in all three zones of undeformed RU is 0.57, and after the deformation is 0.56, which represents a slight decrease (see

Figure 18). For the CN1 specimen, the mean sphericity of the defects in all three zones for undeformed and deformed conditions were 0.57 and 0.55, respectively, which also showed a slight decrease, whereas the standard deviation showed a slight increase in all three zones after fracture. The mean sphericity of the defects in all three zones of CN2 and CN3 specimens in the undeformed condition was 0.56, and it slightly increased after fracture to 0.58, whereas the standard deviation of the sphericity distributions decreased after fracture. In the AM 17-4 stainless specimens, the

sphericity of the smaller defects was found to be higher compared to that of the larger defects and larger defects have usually a more irregular shape than smaller defects (see

Figure 19). The newly nucleated voids are smaller in size with higher sphericity. In the case of CN2 and CN3 specimens, the nucleated voids could not get a chance of enough growth due to the lower fracture strain. However, in RU and CN1 specimens, the nucleated voids also dilated or elongated due to higher fracture strains compared to CN2 and CN3, which could reduce the sphericity of the newly nucleated voids.

## 4.3 Influence of Sudden Geometrical Changes on Size of AM Defects

In the present study, notched specimens were used to investigate the influence of sudden geometric change on the number and density of AM defects. The bar charts providing the void volume fraction in the three zones A, B, and C of all the test specimens are presented in

Figure 20. It is important to note that all three zones in the unnotched specimen RU have a uniform cross-section diameter, whereas Zone A of all the notched specimens has a sudden geometric change, unlike the remaining two zones in the notched specimens. As evident from the bar chart presented in

Figure 20, the void volume fraction in the three zones of each of the notched specimens is similar after fracture, implying that sudden geometric change in AM specimens does not influence the void volume after the fracture. However, based on the images extracted using micro-CT, the zone consisting of sudden geometric change (zone A) in all the undeformed notched specimens was found to have larger defects compared to the other zones in the specimen. This can be observed in the defect size (equivalent spherical diameter) distribution plots where the mean defect size corresponding to zone A in the undeformed notched specimens was higher compared to that of the

other zones in the notched specimens. Furthermore, the largest defect size in the undeformed notched specimens was found in zone A of the specimen. The maximum defect size (equivalent spherical diameter) found in zones A, B, and C of undeformed specimen CN1 are 286.52  $\mu$ m, 172.82  $\mu$ m, and 164.16  $\mu$ m, respectively, implying that the largest void present in zone A is ~1.65 times greater than that of the other zones in the specimen. Similar observations were made for undeformed notched specimens CN2 and CN3 where the maximum defect sizes (equivalent spherical diameter) in zone A are 320.41  $\mu$ m and 386.64  $\mu$ m which are ~1.68 times and ~2.4 times greater than their counterparts in zones B and C of the undeformed specimens. Therefore, it can be concluded that undeformed as-built AM steel specimens with sudden geometric change, such as, the notch root of the notched specimens used in this study, are prone to larger inherent defects, which may result in early fracture initiation in the steel specimens.

# **4.4 Fracture Initiating Mechanism**

In the previous sections, the void counts per unit volume and void volume fraction were observed to increase in the deformed test specimens, thereby indicating void nucleation and void growth, which are the initial stages of ductile fracture. The increase in void counts per cubic millimeter ranged from  $\sim 60\%$  to 145%, and the void volume fraction increased by  $\sim 50\%$  to 62% in the deformed test specimens (see

Figure 21). The final stage of ductile fracture involves the coalescence of the microvoids present in the specimen over a critical length defined as the characteristic length of the material (Kanvinde and Deierlein 2006; Kiran and Khandelwal 2014b). The maximum size of the defects quantified by the equivalent spherical diameter in the deformed specimens is significantly higher than the defects observed in the specimen before fracture (see

Figure 22). The coalesced microvoids were identified using the scanned micro-CT images of the fractured specimens (see

Figure 23). The maximum equivalent spherical diameter of the defects observed in undeformed specimens RU, CN1, CN2, and CN3 are 199  $\mu$ m, 286.52  $\mu$ m, 320.41  $\mu$ m, and 386.64  $\mu$ m, respectively whereas the maximum equivalent spherical diameter of the coalesced defects in the deformed specimens RU, CN1, CN2, and CN3 are 623.02  $\mu$ m, 490.71  $\mu$ m, 391.21  $\mu$ m, and 538.09  $\mu$ m, respectively.

Therefore, the coalesced microvoids observed in the micro-CT images and the increase in the size of the largest defects observed in the specimens after fracture suggest the coalescence of voids in the test specimens, which is the final stage of ductile fracture. The equivalent spherical diameter of these coalesced voids ranges between 350-600 µm, suggesting that the voids coalesce over this critical length to initiate ductile fracture in AM steel specimens. Therefore, the increase in the number of voids, void volume fraction, and the presence of coalesced microvoids in the fractured specimens provide sufficient evidence of ductile fracture in the as-built AM steel test specimens, which is not apparent in the SEM analysis.

#### 5. Conclusions

The following are the important conclusions drawn from this study:

1. The number of voids per cubic millimeter increased by 61.62%, 64.56%, 156.13%, and 145.03% after fracture in specimens RU, CN1, CN2, and CN3, respectively. The increment in void count in all three zones of the test specimens indicates void nucleation under an evolving stress state and plastic strain in the material.

2. The void volume fraction increased by 59%, 52%, 55%, and 45% for specimens RU, CN1, CN2, and CN3. The increase in void volume fraction can be attributed to two phenomena, namely, void nucleation and void growth. It is important to note that the void growth occurs in the newly nucleated voids as well as the inherent AM defects existing in the test specimens.

- 3. The largest defects inherently existing in the AM test specimens were tracked after deformation, which revealed significantly higher volume growth for the largest existing defects after loading compared to the rest of the existing defects. The largest 500 defects grew by 2-11%, and the largest 200 defects grew by 5-13%, indicating chances of premature failure of the AM test specimens associated with a lack of control over the maximum size of inherent AM defects.
  - 4. Geometrical intricacy can inherently result in larger defects in the AM components. Large defects were observed near the notch root, and the equivalent spherical diameters in zone A are ~1.65-2.4 times greater than their counterparts in zones B and C of the undeformed notched specimens, which can be attributed to the sudden change in geometry of the test specimens. Therefore, avoiding and taking special care of AM specimens with abrupt geometrical changes is advisable.
  - 5. The micro-CT scans further captured large, coalesced defects with equivalent spherical diameters of 623 μm, 490 μm, 354 μm, and 538 μm in the deformed specimens RU, CN1, CN2, and CN3, respectively. Coalesced void colonies provide direct evidence of void coalescence in the deformed AM 17-4 steel specimens.
- 6. The micro-CT analysis provided evidence of microvoid nucleation (61-156% increase), dilation (45-59% volume change including the newly nucleated voids), and coalescence

over a length varying between 350-623 microns in the AM 17-4 steel, indicating the ductile fracture as the fracture initiating mechanism. The characteristic length for the damage in the AM steel is around 600 µm based on the analysis of the largest coalesced voids.

488

485

486

487

489

490

491

492

493

494

495

496

497

498

499

500

# **Data Availability Statement**

The raw/processed data required to reproduce these findings cannot be shared at this time as the data also forms part of an ongoing study.

# Acknowledgments

The research presented in this paper was supported by the National Science Foundation under CAREER award # 2045538. Any opinions, findings, conclusions, or recommendations expressed in this material are those of the author(s) and do not necessarily reflect the views of the National Science Foundation.

#### References

- Allen, P. 1945. "Lognormal Distributions." *Nature*, 156 (3973): 746–747. Nature Publishing Group. https://doi.org/10.1038/156746b0.
- Alnajjar, M., F. Christien, C. Bosch, and K. Wolski. 2020. "A comparative study of
- 502 microstructure and hydrogen embrittlement of selective laser melted and wrought 17–
- 4 PH stainless steel." *Materials Science and Engineering: A*, 785: 139363.
- 504 https://doi.org/10.1016/j.msea.2020.139363.
- Avner, S. H. 1974. *Introduction to Physical Metallurgy*. McGraw-Hill.

506 Bai, B., R. Hu, C. Zhang, J. Xue, and W. Yang. 2021. "Effect of precipitates on hardening of 17-507 4PH martensitic stainless steel serviced at 300 °C in nuclear power plant." Annals of Nuclear Energy, 154: 108123. https://doi.org/10.1016/j.anucene.2020.108123. 508 509 Bajaj, P., A. Hariharan, A. Kini, P. Kürnsteiner, D. Raabe, and E. A. Jägle. 2020. "Steels in 510 additive manufacturing: A review of their microstructure and properties." Materials 511 Science and Engineering: A, 772: 138633. https://doi.org/10.1016/j.msea.2019.138633. 512 Berez, J., L. Sheridan, and C. Saldaña. 2022. "Extreme variation in fatigue: Fatigue life 513 prediction and dependence on build volume location in laser powder bed fusion of 17-4 514 stainless steel." International Journal of Fatigue, 158: 106737. https://doi.org/10.1016/j.ijfatigue.2022.106737. 515 516 Blakey-Milner, B., P. Gradl, G. Snedden, M. Brooks, J. Pitot, E. Lopez, M. Leary, F. Berto, and 517 A. du Plessis. 2021. "Metal additive manufacturing in aerospace: A review." *Materials &* Design, 209: 110008. https://doi.org/10.1016/j.matdes.2021.110008. 518 519 Borela, R., J. D. Frost, G. Viggiani, and F. Anselmucci. 2021. "Earthworm-inspired robotic 520 locomotion in sand: an experimental study with X-ray tomography." Géotechnique Letters, 11 (1): 66–73. ICE Publishing. https://doi.org/10.1680/jgele.20.00085. 521 522 Buchanan, C., and L. Gardner. 2019. "Metal 3D printing in construction: A review of methods, research, applications, opportunities and challenges." Engineering Structures, 180: 332– 523 524 348. https://doi.org/10.1016/j.engstruct.2018.11.045. 525 Calle, M. A. G., M. Salmi, L. M. Mazzariol, M. Alves, and P. Kujala. 2020. "Additive manufacturing of miniature marine structures for crashworthiness verification: Scaling 526 527 technique and experimental tests." Marine Structures, 72: 102764. 528 https://doi.org/10.1016/j.marstruc.2020.102764.

529 DebRoy, T., H. L. Wei, J. S. Zuback, T. Mukherjee, J. W. Elmer, J. O. Milewski, A. M. Beese, 530 A. Wilson-Heid, A. De, and W. Zhang. 2018. "Additive manufacturing of metallic components – Process, structure and properties." Progress in Materials Science, 92: 112– 531 224. https://doi.org/10.1016/j.pmatsci.2017.10.001. 532 533 Dennies, D. P. 2021. "Critical Thinking in the Application of Additive Manufacturing Processes: 534 A Review." J Fail. Anal. and Preven., 21 (4): 1099–1125. https://doi.org/10.1007/s11668-021-01175-x. 535 Dey, Surajit, Yellavajjala, Ravi Kiran, and Ulven, Chad. n.d. "Experimental Evaluation of 536 537 Microvoid Characteristics and their Relationship with Stress and Strain for Ductile Fracture." ASCE Journal of Materials in Civil Engineering (Under Review). 538 Dilip, J. J. S., S. Zhang, C. Teng, K. Zeng, C. Robinson, D. Pal, and B. Stucker. 2017. "Influence 539 540 of processing parameters on the evolution of melt pool, porosity, and microstructures in Ti-6Al-4V alloy parts fabricated by selective laser melting." *Prog Addit Manuf*, 2 (3): 541 157–167. https://doi.org/10.1007/s40964-017-0030-2. 542 Eliaz, N., N. Foucks, D. Geva, S. Oren, N. Shriki, D. Vaknin, D. Fishman, and O. Levi. 2020. 543 "Comparative Quality Control of Titanium Alloy Ti-6Al-4V, 17-4 PH Stainless Steel, 544 545 and Aluminum Alloy 4047 Either Manufactured or Repaired by Laser Engineered Net Shaping (LENS)." *Materials*, 13 (18): 4171. Multidisciplinary Digital Publishing 546 547 Institute. https://doi.org/10.3390/ma13184171. 548 Elmoutaouakkil, A., L. Salvo, E. Maire, and G. Peix. 2002. "2D and 3D Characterization of Metal Foams Using X-ray Tomography." Advanced Engineering Materials, 4 (10): 803– 549 550 807. https://doi.org/10.1002/1527-2648(20021014)4:10<803::AID-ADEM803>3.0.CO;2-551 D.

552 Frazier, W. E. 2014. "Metal Additive Manufacturing: A Review." J. of Materi Eng and Perform, 23 (6): 1917–1928. https://doi.org/10.1007/s11665-014-0958-z. 553 Gardner, L. 2023. "Metal additive manufacturing in structural engineering – review, advances, 554 opportunities and outlook." Structures, 47: 2178–2193. 555 https://doi.org/10.1016/j.istruc.2022.12.039. 556 557 Gong, H., K. Rafi, H. Gu, G. D. Janaki Ram, T. Starr, and B. Stucker. 2015. "Influence of defects on mechanical properties of Ti-6Al-4V components produced by selective laser 558 melting and electron beam melting." *Materials & Design*, 86: 545–554. 559 560 https://doi.org/10.1016/j.matdes.2015.07.147. Gonzalez-Nino, D., S. Sonntag, M. Afshar-Mohajer, J. Goss, M. Zou, and G. S. Prinz. 2021a. 561 "Micromechanical Tension Testing of Additively Manufactured 17-4 PH Stainless Steel 562 563 Specimens." JoVE (Journal of Visualized Experiments), (170): e62433. https://doi.org/10.3791/62433. 564 Gonzalez-Nino, D., T. Strasser, and G. S. Prinz. 2021b. "Ultra Low-Cycle Fatigue Behavior 565 Comparison between Additively Manufactured and Rolled 17-4 PH (AISI 630) Stainless 566 Steels." *Metals*, 11 (11): 1726. Multidisciplinary Digital Publishing Institute. 567 568 https://doi.org/10.3390/met11111726. He, P., W. Du, L. Wang, R. Kiran, and M. Yang. 2020. "Additive Manufacturing and 569 570 Mechanical Performance of Trifurcated Steel Joints for Architecturally Exposed Steel 571 Structures." *Materials*, 13 (8): 1901. https://doi.org/10.3390/ma13081901. Huang, L., Y. Cao, H. Zhao, Y. Li, Y. Wang, and L. Wei. 2022. "Effect of process parameters on 572 573 density and mechanical behaviour of a selective laser melted 17-4PH stainless steel

574 alloy." Open Physics, 20 (1): 66–77. De Gruyter Open Access. https://doi.org/10.1515/phys-2022-0008. 575 Jasiuk, I., D. W. Abueidda, C. Kozuch, S. Pang, F. Y. Su, and J. McKittrick. 2018. "An 576 Overview on Additive Manufacturing of Polymers." JOM, 70 (3): 275–283. 577 https://doi.org/10.1007/s11837-017-2730-y. 578 579 Jiang, T., J. Zhong, X. Zhang, W. Wang, and K. Guan. 2020. "Hydrogen embrittlement induced fracture of 17-4 PH stainless steel valve stem." Engineering Failure Analysis, 113: 580 581 104576. https://doi.org/10.1016/j.engfailanal.2020.104576. 582 Kanvinde, A. M., and G. G. Deierlein. 2006. "The Void Growth Model and the Stress Modified Critical Strain Model to Predict Ductile Fracture in Structural Steels." Journal of 583 Structural Engineering, 132 (12): 1907–1918. American Society of Civil Engineers. 584 585 https://doi.org/10.1061/(ASCE)0733-9445(2006)132:12(1907). Kanyilmaz, A., A. G. Demir, M. Chierici, F. Berto, L. Gardner, S. Y. Kandukuri, P. Kassabian, 586 587 T. Kinoshita, A. Laurenti, I. Paoletti, A. du Plessis, and N. Razavi. 2022. "Role of metal 3D printing to increase quality and resource-efficiency in the construction sector." 588 Additive Manufacturing, 50: 102541. https://doi.org/10.1016/j.addma.2021.102541. 589 590 Khosravani, M. R., P. Soltani, K. Weinberg, and T. Reinicke. 2021. "Structural integrity of 591 adhesively bonded 3D-printed joints." *Polymer Testing*, 100: 107262. 592 https://doi.org/10.1016/j.polymertesting.2021.107262. 593 Kim, K. Y., T. S. Yun, J. Choo, D. H. Kang, and H. S. Shin. 2012. "Determination of air-void parameters of hardened cement-based materials using X-ray computed tomography." 594 595 Construction and Building Materials, Non Destructive Techniques for Assessment of 596 Concrete, 37: 93–101. https://doi.org/10.1016/j.conbuildmat.2012.07.012.

597 King, W. E., A. T. Anderson, R. M. Ferencz, N. E. Hodge, C. Kamath, S. A. Khairallah, and A. M. Rubenchik. 2015. "Laser powder bed fusion additive manufacturing of metals; 598 physics, computational, and materials challenges." Applied Physics Reviews, 2 (4): 599 041304. American Institute of Physics. https://doi.org/10.1063/1.4937809. 600 Kiran, R., and K. Khandelwal. 2013. "A micromechanical model for ductile fracture prediction 601 602 in ASTM A992 steels." Engineering Fracture Mechanics, 102: 101–117. https://doi.org/10.1016/j.engfracmech.2013.02.021. 603 Kiran, R., and K. Khandelwal. 2014a. "Experimental Studies and Models for Ductile Fracture in 604 605 ASTM A992 Steels at High Triaxiality." *Journal of Structural Engineering*, 140 (2): 04013044. American Society of Civil Engineers. 606 https://doi.org/10.1061/(ASCE)ST.1943-541X.0000828. 607 608 Kiran, R., and K. Khandelwal. 2014b. "Experimental Studies and Models for Ductile Fracture in ASTM A992 Steels at High Triaxiality." Journal of Structural Engineering, 140 (2): 609 610 04013044. American Society of Civil Engineers. https://doi.org/10.1061/(ASCE)ST.1943-541X.0000828. 611 Kuwamura, H., and K. Yamamoto. 1997. "Ductile Crack as Trigger of Brittle Fracture in Steel." 612 613 Journal of Structural Engineering, 123 (6): 729–735. American Society of Civil Engineers. https://doi.org/10.1061/(ASCE)0733-9445(1997)123:6(729). 614 615 Limpert, E., W. A. Stahel, and M. Abbt. 2001. "Log-normal Distributions across the Sciences: 616 Keys and Clues: On the charms of statistics, and how mechanical models resembling gambling machines offer a link to a handy way to characterize log-normal distributions, 617 618 which can provide deeper insight into variability and probability—normal or log-normal: 619 That is the question." BioScience, 51 (5): 341–352. https://doi.org/10.1641/0006-3568(2001)051[0341:LNDATS]2.0.CO;2. 620 Mattey, R., B. Jewell, S. Ghosh, and T. Sain. 2023. "Phase-field fracture coupled elasto-plastic 621 constitutive model for 3D printed thermoplastics and composites." Engineering Fracture 622 Mechanics, 291: 109535. https://doi.org/10.1016/j.engfracmech.2023.109535. 623 624 Meng, L. X., D. D. Ben, H. J. Yang, H. B. Ji, D. L. Lian, Y. K. Zhu, J. Chen, J. L. Yi, L. Wang, J. B. Yang, and Z. F. Zhang. 2021. "Effects of embedded spherical pore on the tensile 625 626 properties of a selective laser melted Ti6Al4V alloy." Materials Science and 627 Engineering: A, 815: 141254. https://doi.org/10.1016/j.msea.2021.141254. Mostafaei, A., C. Zhao, Y. He, S. Reza Ghiaasiaan, B. Shi, S. Shao, N. Shamsaei, Z. Wu, N. 628 629 Kouraytem, T. Sun, J. Pauza, J. V. Gordon, B. Webler, N. D. Parab, M. Asherloo, Q. 630 Guo, L. Chen, and A. D. Rollett. 2022. "Defects and anomalies in powder bed fusion metal additive manufacturing." Current Opinion in Solid State and Materials Science, 26 631 632 (2): 100974. https://doi.org/10.1016/j.cossms.2021.100974. Naik, D. L., and R. Kiran. 2019. "Identification and characterization of fracture in metals using 633 machine learning based texture recognition algorithms." Engineering Fracture 634 635 Mechanics, 219: 106618. https://doi.org/10.1016/j.engfracmech.2019.106618. Naik, D. L., H. U. Sajid, and R. Kiran. 2019. "Texture-Based Metallurgical Phase Identification 636 637 in Structural Steels: A Supervised Machine Learning Approach." *Metals*, 9 (5): 546. 638 https://doi.org/10.3390/met9050546. Pineau, A., A. A. Benzerga, and T. Pardoen. 2016. "Failure of metals I: Brittle and ductile 639 640 fracture." Acta Materialia, 107: 424–483. https://doi.org/10.1016/j.actamat.2015.12.034.

Rezvani Ghomi, E., F. Khosravi, R. E. Neisiany, S. Singh, and S. Ramakrishna. 2021. "Future of 641 additive manufacturing in healthcare." Current Opinion in Biomedical Engineering, 17: 642 100255. https://doi.org/10.1016/j.cobme.2020.100255. 643 Roy, N., J. D. Frost, and G. Viggiani. 2022. "Pore space evolution of granular assemblies under 644 shear: an experimental study using X-ray tomography." Granular Matter, 24 (2): 63. 645 646 https://doi.org/10.1007/s10035-022-01225-7. Sajid, H. U., and R. Kiran. 2018. "Influence of high stress triaxiality on mechanical strength of 647 ASTM A36, ASTM A572 and ASTM A992 steels." Construction and Building 648 649 Materials, 176: 129–134. https://doi.org/10.1016/j.conbuildmat.2018.05.018. Sajid, H. U., D. L. Naik, and R. Kiran. 2020. "Microstructure–Mechanical Property 650 Relationships for Post-Fire Structural Steels." Journal of Materials in Civil Engineering, 651 652 32 (6): 04020133. American Society of Civil Engineers. 653 https://doi.org/10.1061/(ASCE)MT.1943-5533.0003190. 654 Sanaei, N., and A. Fatemi. 2021. "Defects in additive manufactured metals and their effect on fatigue performance: A state-of-the-art review." *Progress in Materials Science*, 117: 655 100724. https://doi.org/10.1016/j.pmatsci.2020.100724. 656 657 Sanaei, N., A. Fatemi, and N. Phan. 2019. "Defect characteristics and analysis of their variability in metal L-PBF additive manufacturing." Materials & Design, 182: 108091. 658 659 https://doi.org/10.1016/j.matdes.2019.108091. 660 Shao, S., M. J. Mahtabi, N. Shamsaei, and S. M. Thompson. 2017. "Solubility of argon in laser additive manufactured α-titanium under hot isostatic pressing condition." Computational 661 662 Materials Science, 131: 209–219. https://doi.org/10.1016/j.commatsci.2017.01.040.

663 Singh, R., Rishab, and J. S. Sidhu. 2022. "On three-dimensional printing of 17-4 precipitationhardenable stainless steel with direct metal laser sintering in aircraft structural 664 applications." Proceedings of the Institution of Mechanical Engineers, Part L: Journal of 665 Materials: Design and Applications, 236 (2): 440–450. SAGE Publications. 666 https://doi.org/10.1177/14644207211044804. 667 668 Singla, A. K., M. Banerjee, A. Sharma, J. Singh, A. Bansal, M. K. Gupta, N. Khanna, A. S. Shahi, and D. K. Goyal. 2021. "Selective laser melting of Ti6Al4V alloy: Process 669 670 parameters, defects and post-treatments." Journal of Manufacturing Processes, 64: 161– 671 187. https://doi.org/10.1016/j.jmapro.2021.01.009. Soja, A., J. Li, S. Tredinnick, and T. Woodfield. 2020. "Surface finishing of additively 672 manufactured stainless steel surgical instruments." Rapid Prototyping Journal, 27 (1): 673 674 59–70. Emerald Publishing Limited. https://doi.org/10.1108/RPJ-01-2020-0009. Sun, Y., R. J. Hebert, and M. Aindow. 2018. "Effect of heat treatments on microstructural 675 676 evolution of additively manufactured and wrought 17-4PH stainless steel." Materials & Design, 156: 429–440. https://doi.org/10.1016/j.matdes.2018.07.015. 677 Suri, P., B. P. Smarslok, and R. M. German. 2006. "Impact properties of sintered and wrought 678 679 17–4 PH stainless steel." *Powder Metallurgy*, 49 (1): 40–47. Taylor & Francis. 680 https://doi.org/10.1179/174329006X89317. Vasco, J. C. 2021. "Chapter 16 - Additive manufacturing for the automotive industry." Additive 681 682 Manufacturing, Handbooks in Advanced Manufacturing, J. Pou, A. Riveiro, and J. P. 683 Davim, eds., 505–530. Elsevier. 684 Wang, L. B., J. D. Frost, and J. S. Lai. 2004. "Three-Dimensional Digital Representation of 685 Granular Material Microstructure from X-Ray Tomography Imaging." *Journal of* 

- 686 Computing in Civil Engineering, 18 (1): 28–35. American Society of Civil Engineers.
- 687 https://doi.org/10.1061/(ASCE)0887-3801(2004)18:1(28).
- Wang, L., and D. J. Frost. 2012. "Quantification of the Specific Aggregate Surface Area Using
- K-Ray Tomography." 3–17. American Society of Civil Engineers.
- 690 https://doi.org/10.1061/40709(257)1.
- Wen, H., and H. Mahmoud. 2016. "New Model for Ductile Fracture of Metal Alloys. I:
- Monotonic Loading." Journal of Engineering Mechanics, 142 (2): 04015088. American
- 693 Society of Civil Engineers. https://doi.org/10.1061/(ASCE)EM.1943-7889.0001009.
- Wilson-Heid, A. E., T. C. Novak, and A. M. Beese. 2019. "Characterization of the Effects of
- Internal Pores on Tensile Properties of Additively Manufactured Austenitic Stainless
- 696 Steel 316L." *Exp Mech*, 59 (6): 793–804. https://doi.org/10.1007/s11340-018-00465-0.
- Wits, W. W., S. Carmignato, F. Zanini, and T. H. J. Vaneker. 2016. "Porosity testing methods
- for the quality assessment of selective laser melted parts." CIRP Annals, 65 (1): 201–204.
- https://doi.org/10.1016/j.cirp.2016.04.054.
- 700 Wu, J.-H., and C.-K. Lin. 2002. "Tensile and fatigue properties of 17-4 PH stainless steel at high
- 701 temperatures." *Metall Mater Trans A*, 33 (6): 1715–1724. https://doi.org/10.1007/s11661-
- 702 002-0180-8.
- Wu, P., J. Wang, and X. Wang. 2016. "A critical review of the use of 3-D printing in the
- construction industry." *Automation in Construction*, 68: 21–31.
- 705 https://doi.org/10.1016/j.autcon.2016.04.005.
- Xu, W., M. Brandt, S. Sun, J. Elambasseril, Q. Liu, K. Latham, K. Xia, and M. Qian. 2015.
- "Additive manufacturing of strong and ductile Ti–6Al–4V by selective laser melting via

708	in situ martensite decomposition." Acta Materialia, 85: 74–84.
709	https://doi.org/10.1016/j.actamat.2014.11.028.
710	Ye, D., J. Li, W. Jiang, J. Su, and K. Zhao. 2012. "Effect of Cu addition on microstructure and
711	mechanical properties of 15%Cr super martensitic stainless steel." Materials & Design,
712	41: 16–22. https://doi.org/10.1016/j.matdes.2012.04.036.
713	Zaefferer, S., NN. Elhami, and P. Konijnenberg. 2012. "18 - Electron backscatter diffraction
714	(EBSD) techniques for studying phase transformations in steels." Phase Transformations
715	in Steels, Woodhead Publishing Series in Metals and Surface Engineering, E. Pereloma
716	and D. V. Edmonds, eds., 557–587. Woodhead Publishing.
717	Ziccarelli, A., A. Kanvinde, and G. Deierlein. 2023. "Cyclic adaptive cohesive zone model to
718	simulate ductile crack propagation in steel structures due to ultra-low cycle fatigue."
719	Fatigue & Fracture of Engineering Materials & Structures, 46 (5): 1821–1836.
720	https://doi.org/10.1111/ffe.13964.
721	

723	List of Tables
724	Table 1. Chemical composition of 17-4 stainless steel powder.
725 726	Table 2. Mean, median, and standard deviation for equivalent spherical diameter of defects in different zones of undeformed and deformed test specimens.
727 728	Table 3. Median, 90th percentile, and 95th percentile equivalent spherical diameter of defects in zone A of undeformed and deformed test specimens.
729 730	Table 4. Mean, median, and standard deviation for sphericity of defects in different zones of undeformed and deformed test specimens.
731	
732	

# 733 List of Figures

- Figure 1. Optical micrograph of the 17-4 AM stainless steel parallel to the build direction.
- Figure 2. SEM microstructures of the 17-4 AM stainless steel obtained on the (a) cross-section
- 736 (perpendicular to the build direction) and (b) vertical section (parallel to the build direction).
- Figure 3. EBSD orientation maps of the 17-4 AM stainless steel specimen obtained along the (a)
- cross-section (perpendicular to the build direction) and (b) vertical section (parallel to the build
- direction). The inverse pole figures are applicable to both sections.
- Figure 4. Geometric details of test specimens. RU-reference unnotched, CN- circular notches.
- Figure 5. Additively manufactured 17-4 test specimens subjected to uniaxial tensions tests
- Figure 6. Engineering stress-strain curves of AM fracture specimens.
- Figure 7. Typical mesh used to discretize (a) an unnotched specimen; (b) a C-notch specimen.
- Figure 8. (a) Strain hardening curve of reference unnotched AM 17-4 steel specimen, and (b) the
- comparison between experimental and FEM stress-strain curves of reference unnotched
- specimen.
- Figure 9. Triaxiality profiles at fracture for as-built AM 17-4 stainless steel specimens.
- Figure 10. Equivalent plastic strain profiles at fracture for as-built AM 17-4 stainless steel
- 749 specimens.
- 750 Figure 11. SEM analysis of the fracture surface of the AM unnotched 17-4 stainless steel
- 751 specimen.
- 752 Figure 12. SEM analysis of the fracture surface of the AM notched 17-4 stainless steel specimen
- 753 CN1 (notch radius 0.5 mm).
- 754 Figure 13. SEM analysis of the fracture surface of conventional unnotched 17-4 PH stainless
- steel specimen. Distinctive microscopic and cones are visible.
- Figure 14. Zones for Micro-CT scan of (a) untested and (b) tested AM steel specimens.
- 757 Figure 15. Comparison of average void count per unit volume for undeformed and fractured AM
- 758 17-4 steel specimens.
- 759 Figure 16. Comparison of average defect volume fraction for undeformed and fractured AM 17-4
- steel specimens.
- Figure 17. Distribution of equivalent spherical defect diameter of the unnotched specimen. (a)
- undeformed zone A, (b) deformed zone A, (c) undeformed zone B, (d) deformed zone B, (e)
- undeformed zone C, and (f) deformed zone C.

- Figure 18. Distribution of sphericity of defects in the unnotched specimen. (a) Undeformed zone
- A, (b) deformed zone A, (c) undeformed zone B, (d) deformed zone B, (e) undeformed zone C,
- and (f) deformed zone C.
- Figure 19. Relationship between sphericity and equivalent spherical diameter for unnotched
- undeformed AM 17-4 steel specimen.
- Figure 20. Comparison of the local void volume fraction in undeformed and deformed test
- specimens.
- Figure 21. Comparison of the void count per unit volume in undeformed and deformed test
- specimens.
- Figure 22. Defects in zone A before and after fracture for specimens (a,b) RU and (c,d) CN1.
- Figure 23. Defects in zone A of deformed test specimens (a) RU, (b) CN1, (c) CN2, and (d)
- 775 CN3.

794 Figures

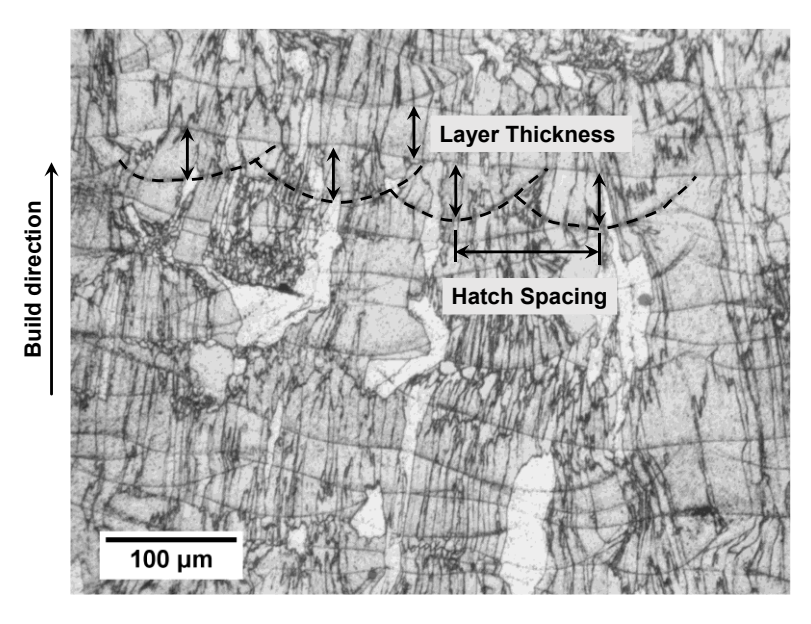


Figure 1. Optical micrograph of the 17-4 AM stainless steel parallel to the build direction.

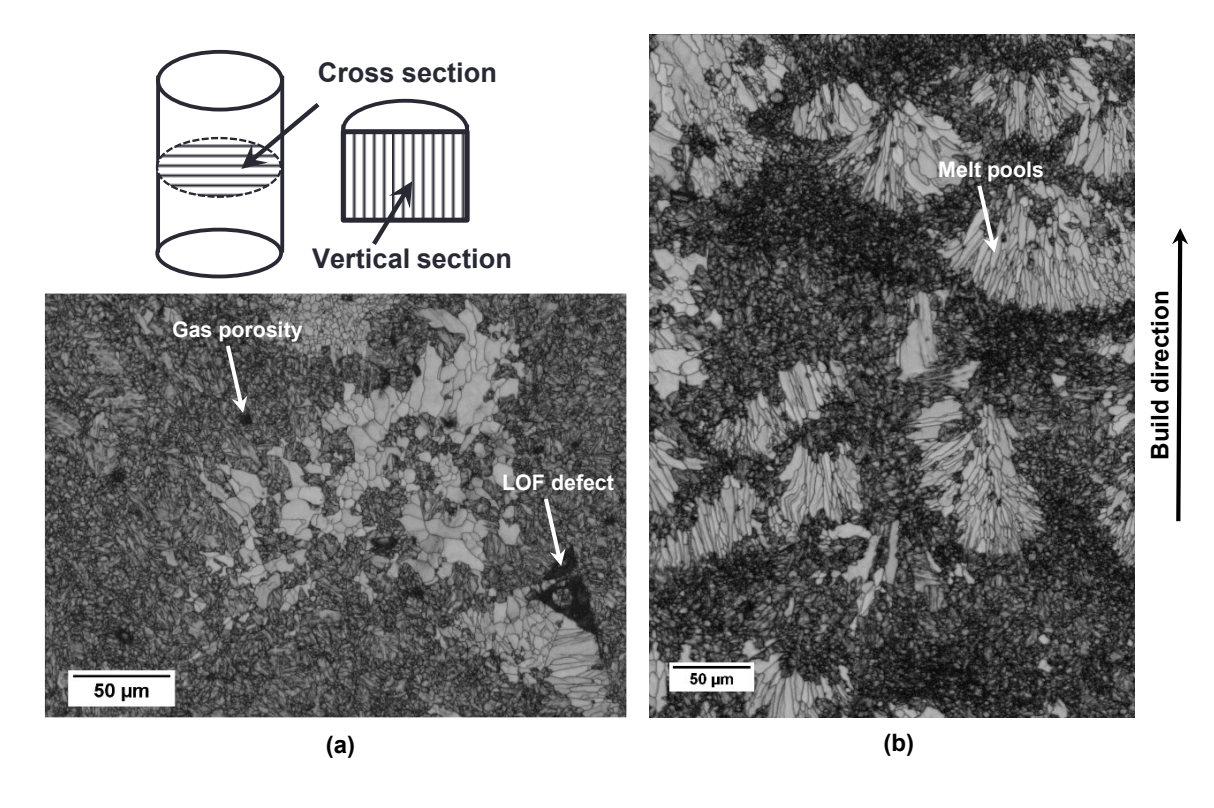


Figure 2. SEM microstructures of the 17-4 AM stainless steel obtained on the (a) cross-section (perpendicular to the build direction) and (b) vertical section (parallel to the build direction).

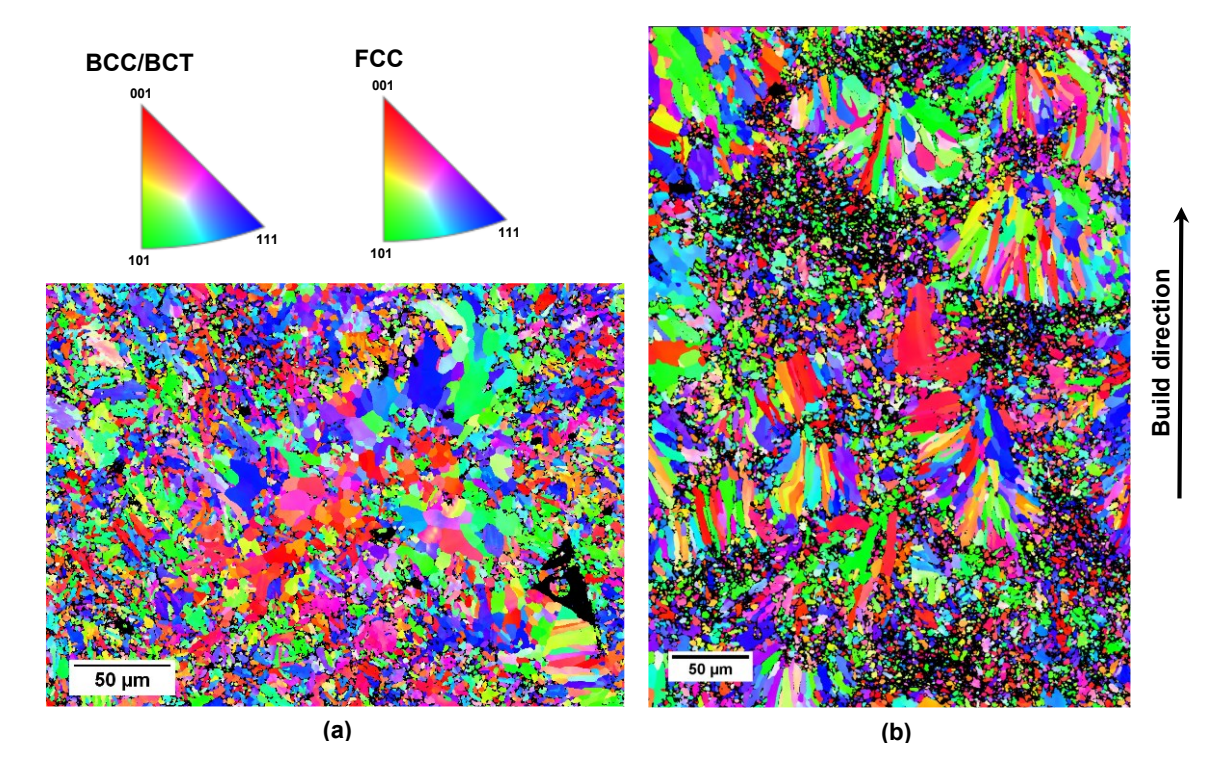


Figure 3. EBSD orientation maps of the 17-4 AM stainless steel specimen obtained along the (a) cross-section (perpendicular to the build direction) and (b) vertical section (parallel to the build direction). The inverse pole figures are applicable to both sections.

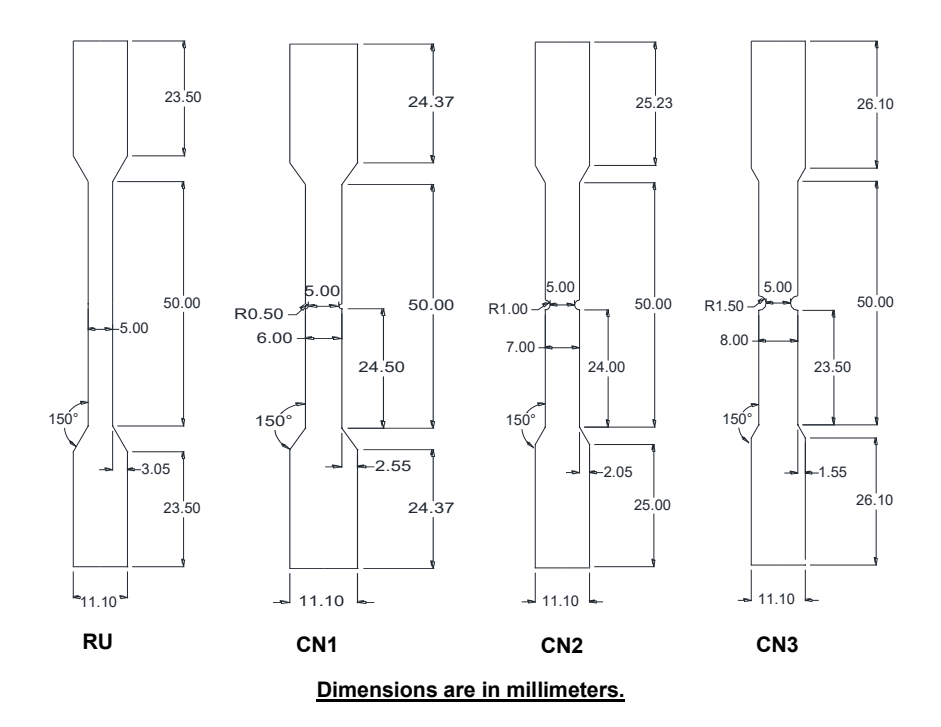


Figure 4. Geometric details of test specimens. RU-reference unnotched, CN- circular notches.



Figure 5: Additively manufactured 17-4 test specimens subjected to uniaxial tensions tests

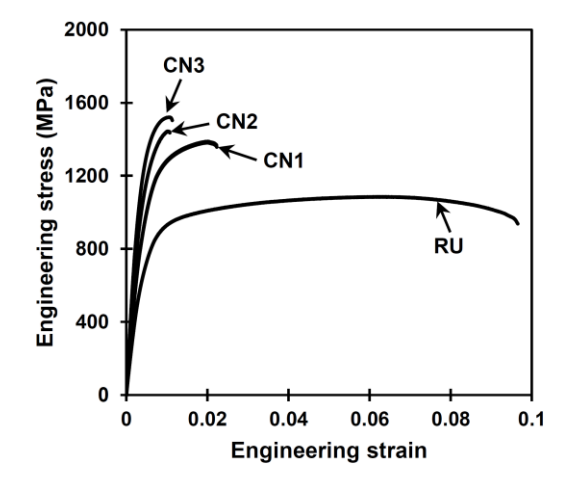


Figure 6. Engineering stress-strain curves of AM fracture specimens.

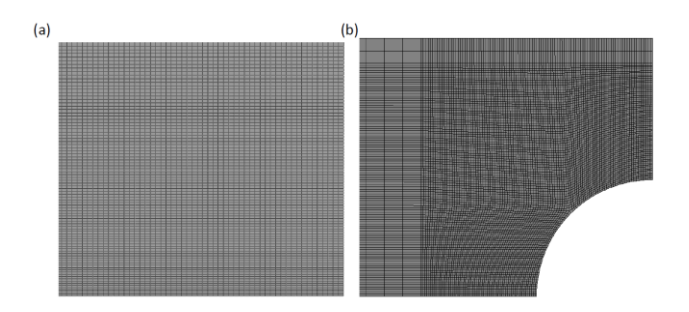


Figure 7: Typical mesh used to discretize (a) an unnotched specimen; (b) a C-notch specimen



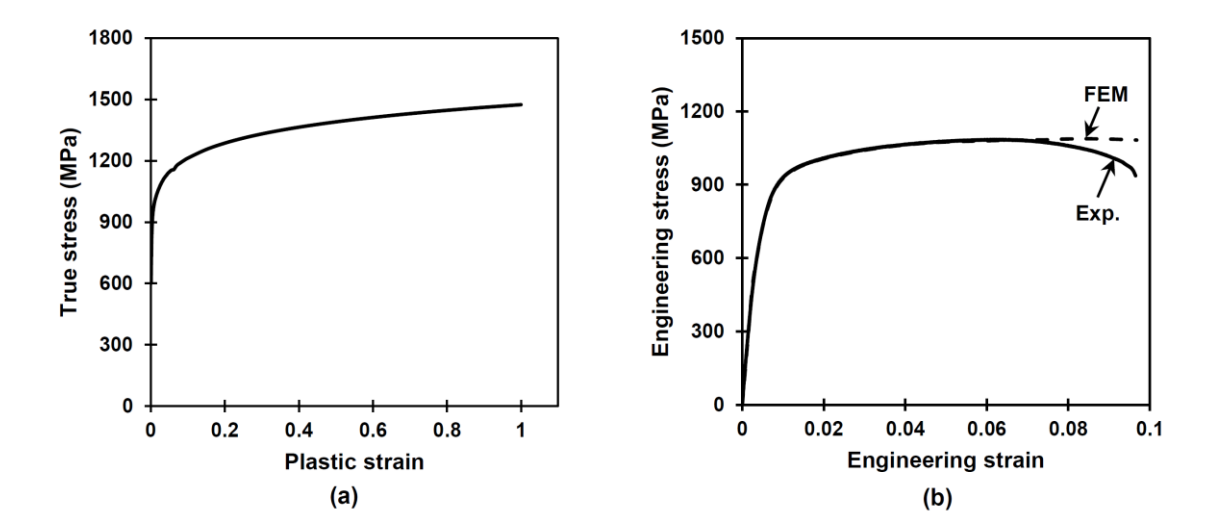


Figure 8. (a) Strain hardening curve of reference unnotched AM 17-4 steel specimen, and (b) the comparison between experimental and FEM stress-strain curves of reference unnotched specimen.

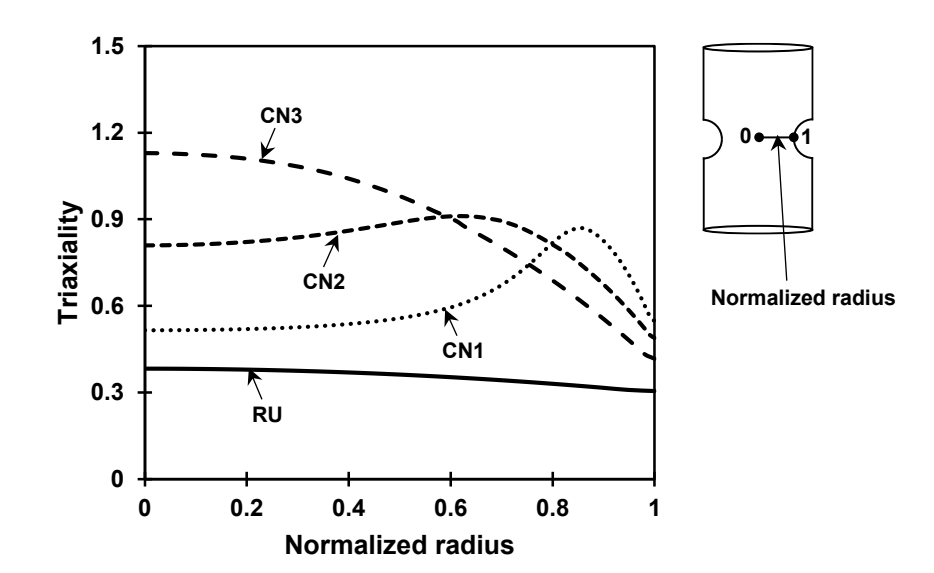


Figure 9. Triaxiality profiles at fracture for as-built AM 17-4 stainless steel specimens.

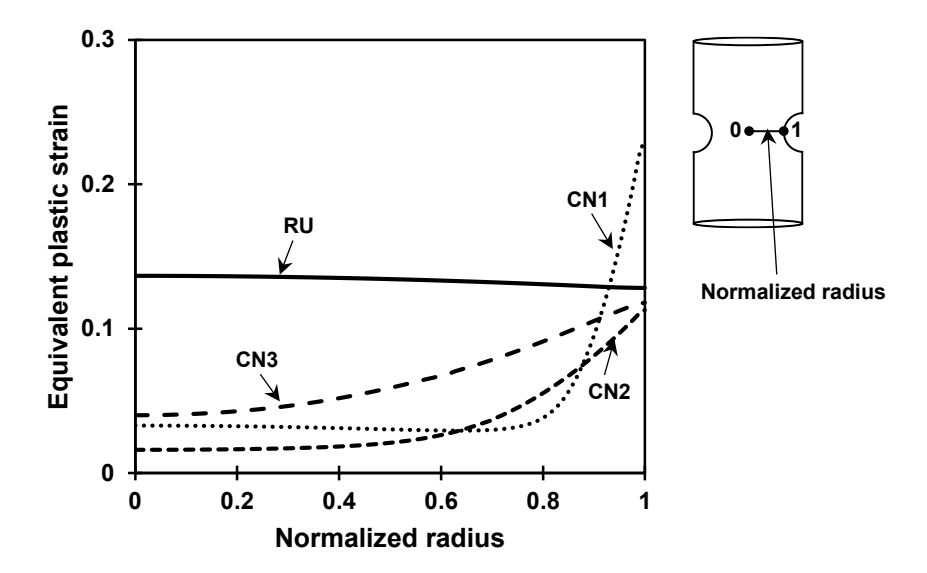


Figure 10. Equivalent plastic strain profiles at fracture for as-built AM 17-4 stainless steel specimens.

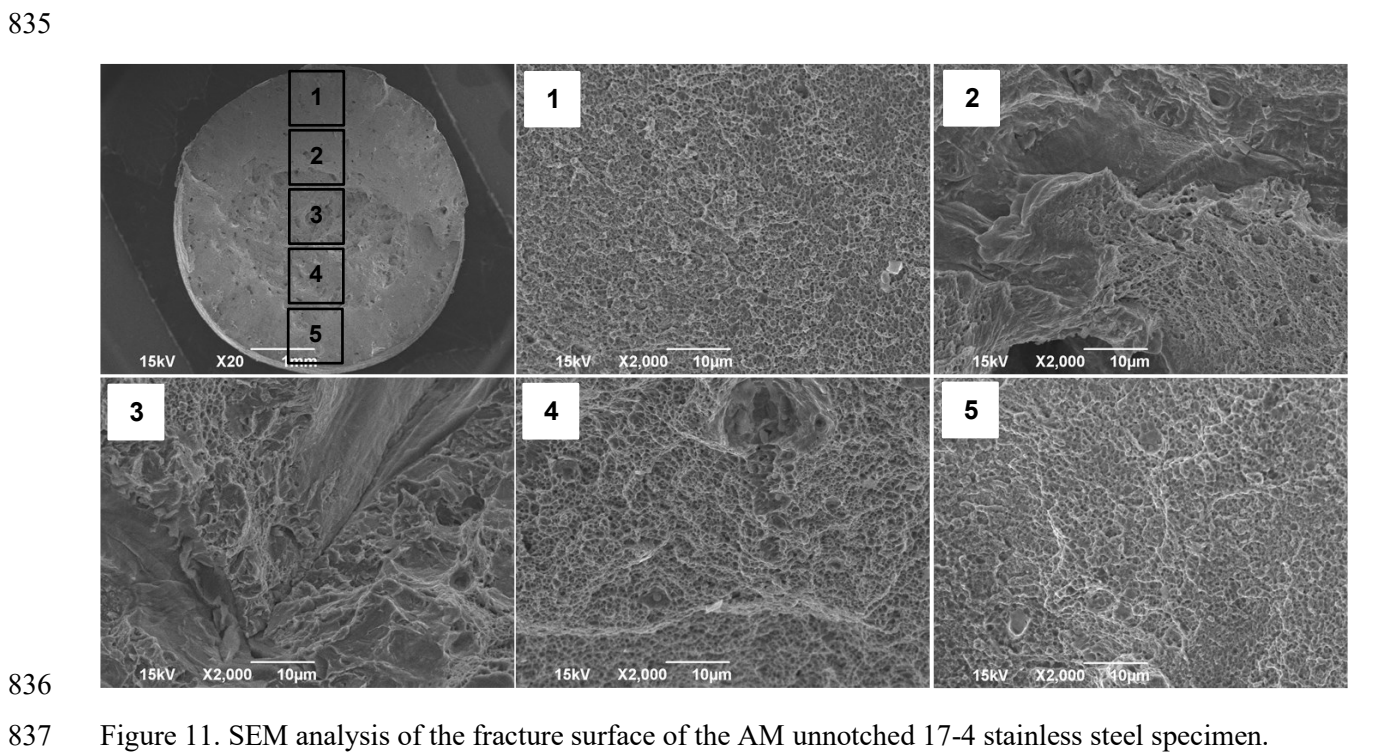


Figure 11. SEM analysis of the fracture surface of the AM unnotched 17-4 stainless steel specimen.

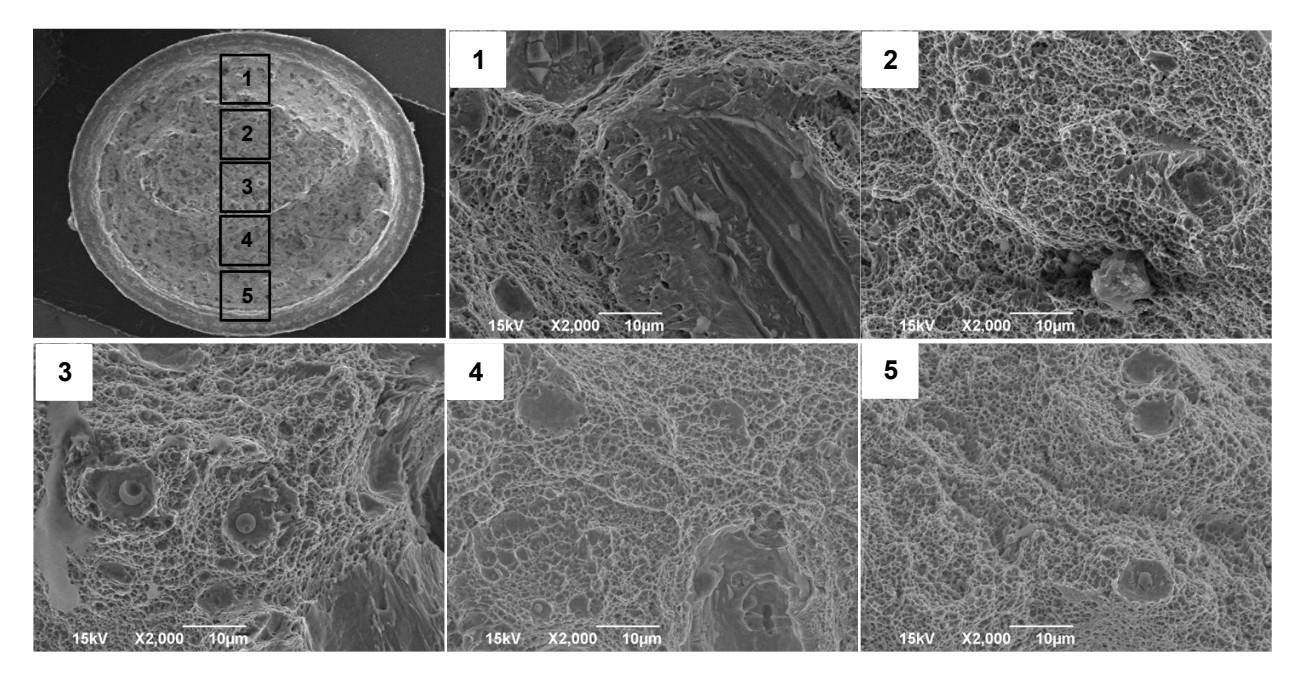


Figure 12. SEM analysis of the fracture surface of the AM notched 17-4 stainless steel specimen CN1 (notch radius 0.5 mm).

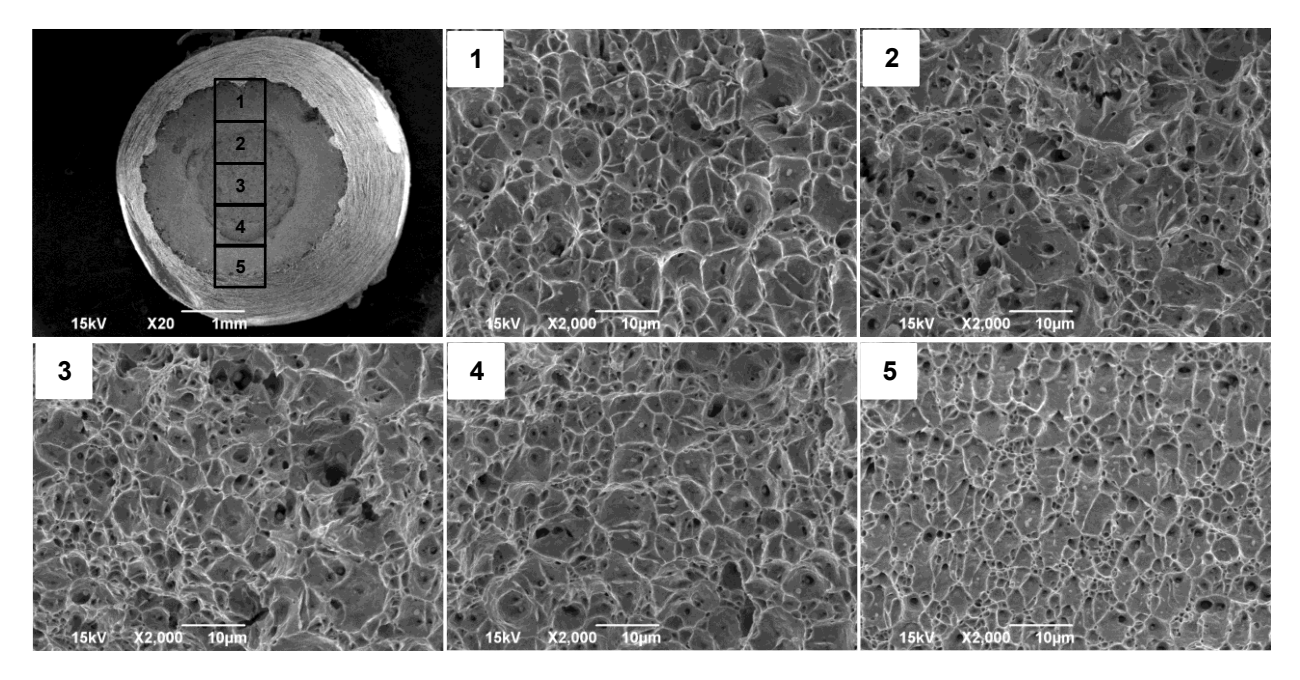
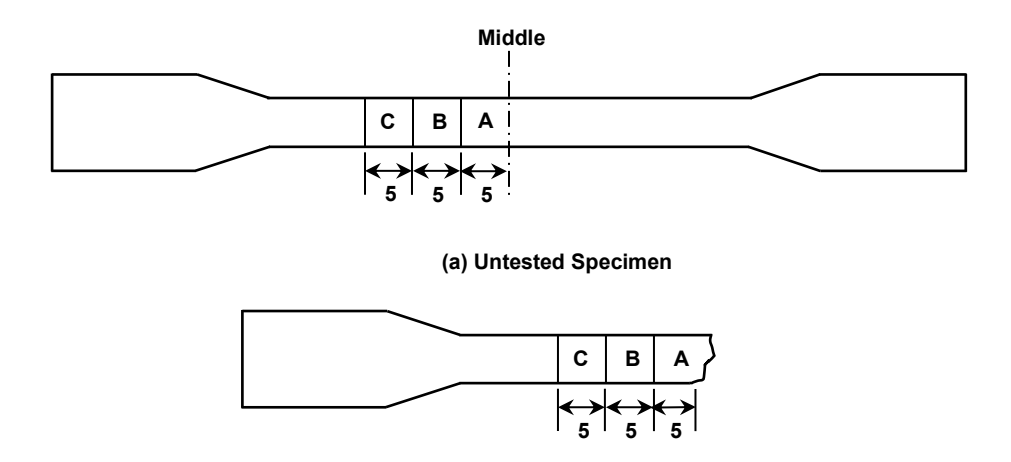


Figure 13. SEM analysis of the fracture surface of conventional unnotched 17-4 PH stainless steel specimen. Distinctive microscopic and cones are visible.





(b) Tested Specimen

## Dimensions are in millimeters.

Figure 14. Zones for Micro-CT scan of (a) untested and (b) tested AM steel specimens.

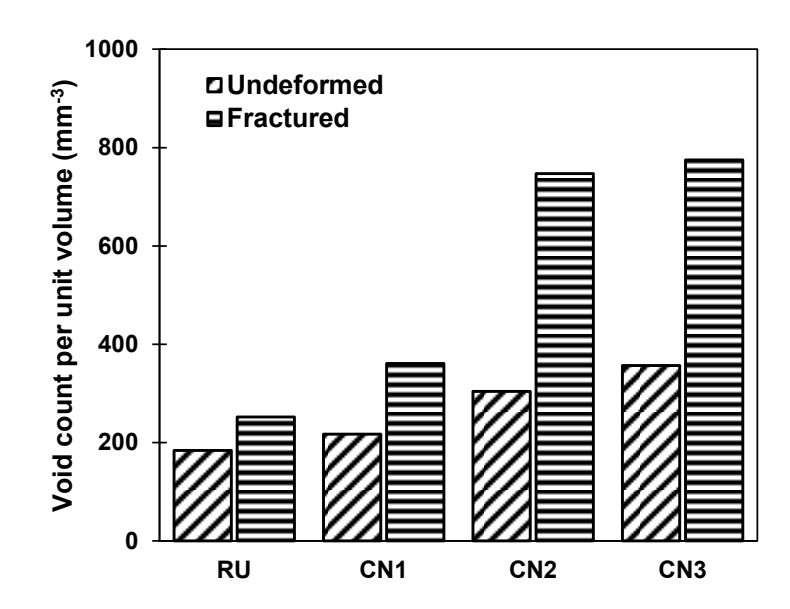


Figure 15. Comparison of average void count per unit volume for undeformed and fractured AM 17-4 steel specimens.

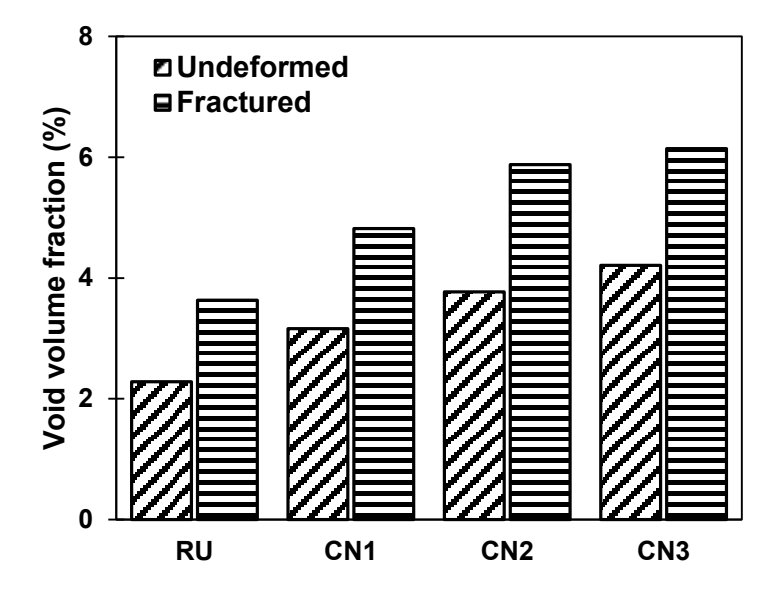


Figure 16. Comparison of average defect volume fraction for undeformed and fractured AM 17-4 steel specimens.



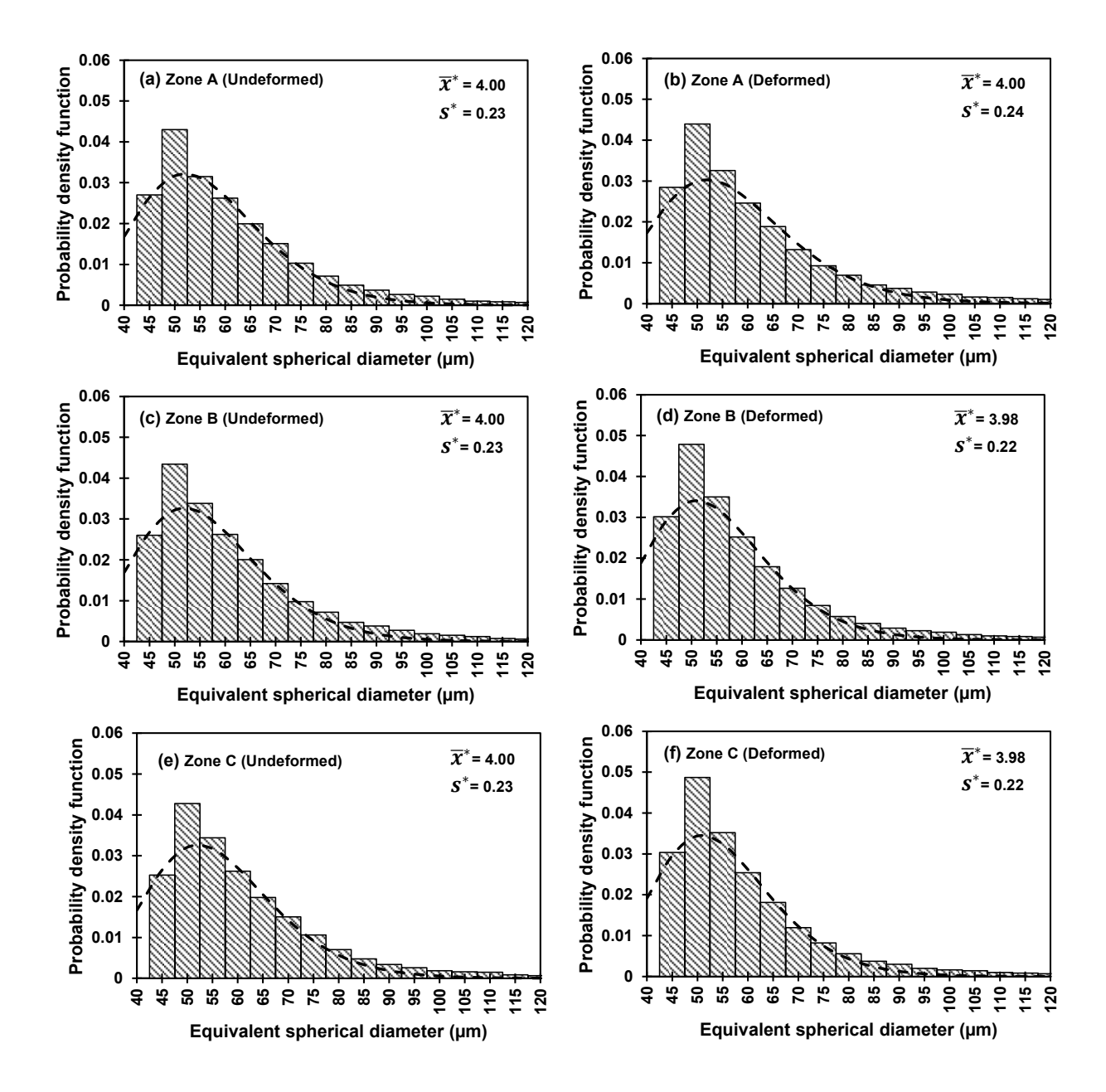


Figure 17. Distribution of equivalent spherical defect diameter of the unnotched specimen. (a) undeformed zone A, (b) deformed zone A, (c) undeformed zone B, (d) deformed zone B, (e) undeformed zone C, and (f) deformed zone C.

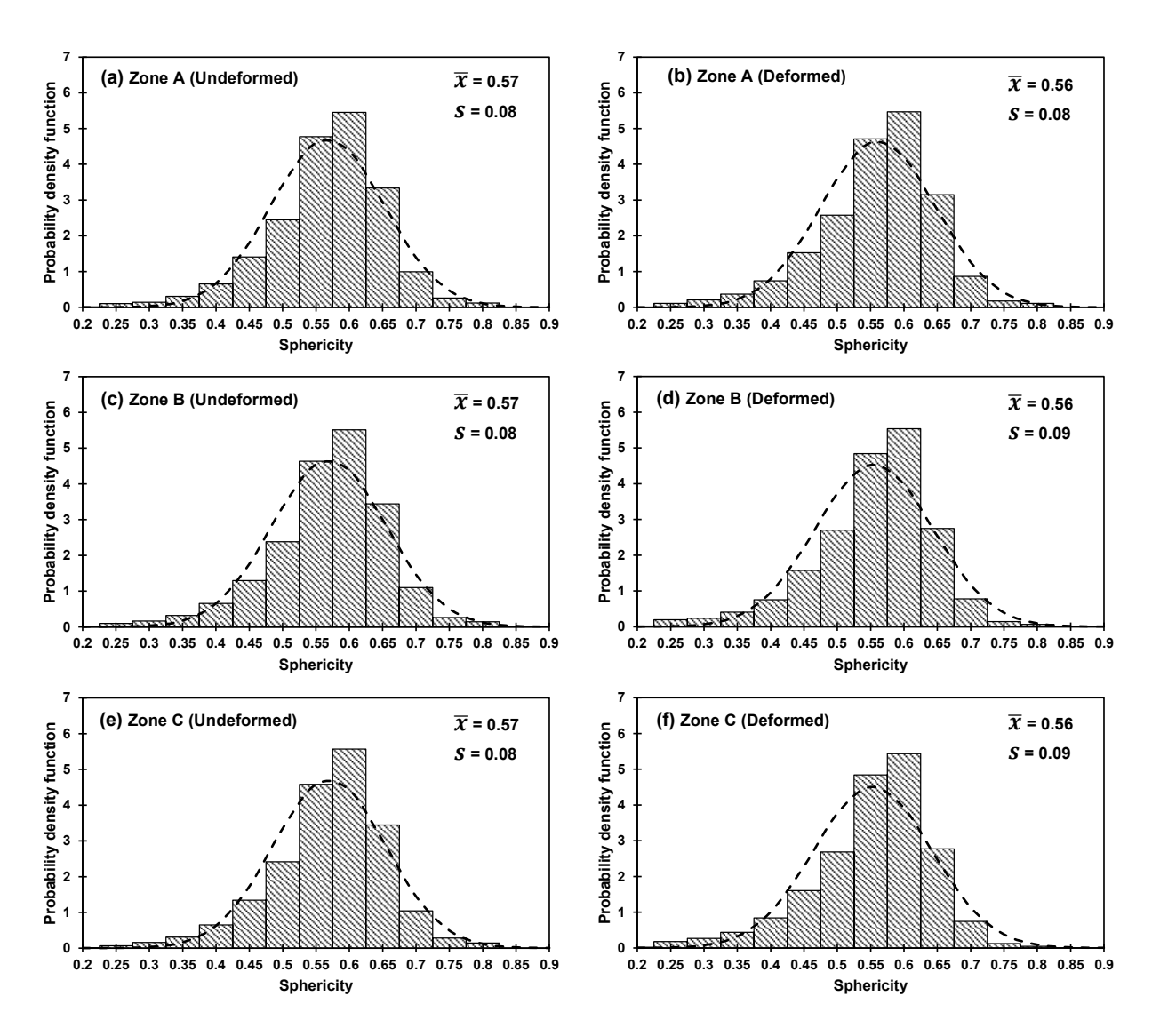


Figure 18. Distribution of sphericity of defects in the unnotched specimen. (a) Undeformed zone A, (b) deformed zone A, (c) undeformed zone B, (d) deformed zone B, (e) undeformed zone C, and (f) deformed zone C.

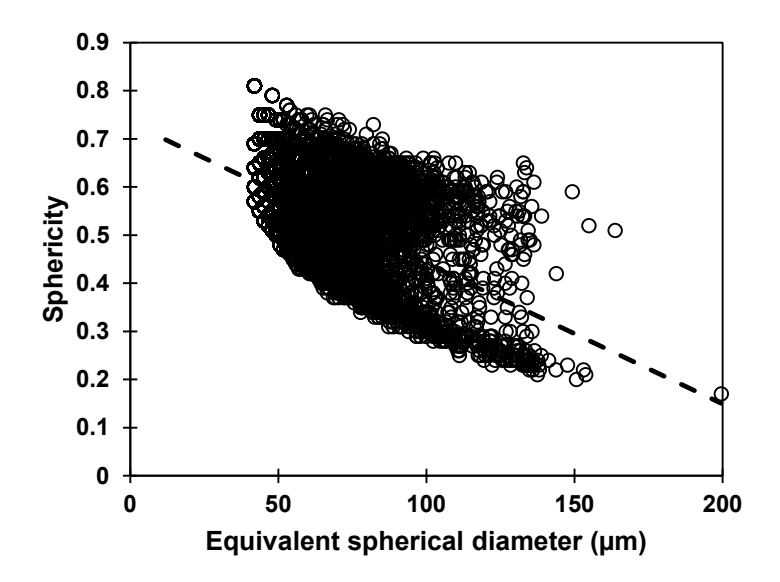


Figure 19. Relationship between sphericity and equivalent spherical diameter for unnotched undeformed AM 17-4 steel specimen.

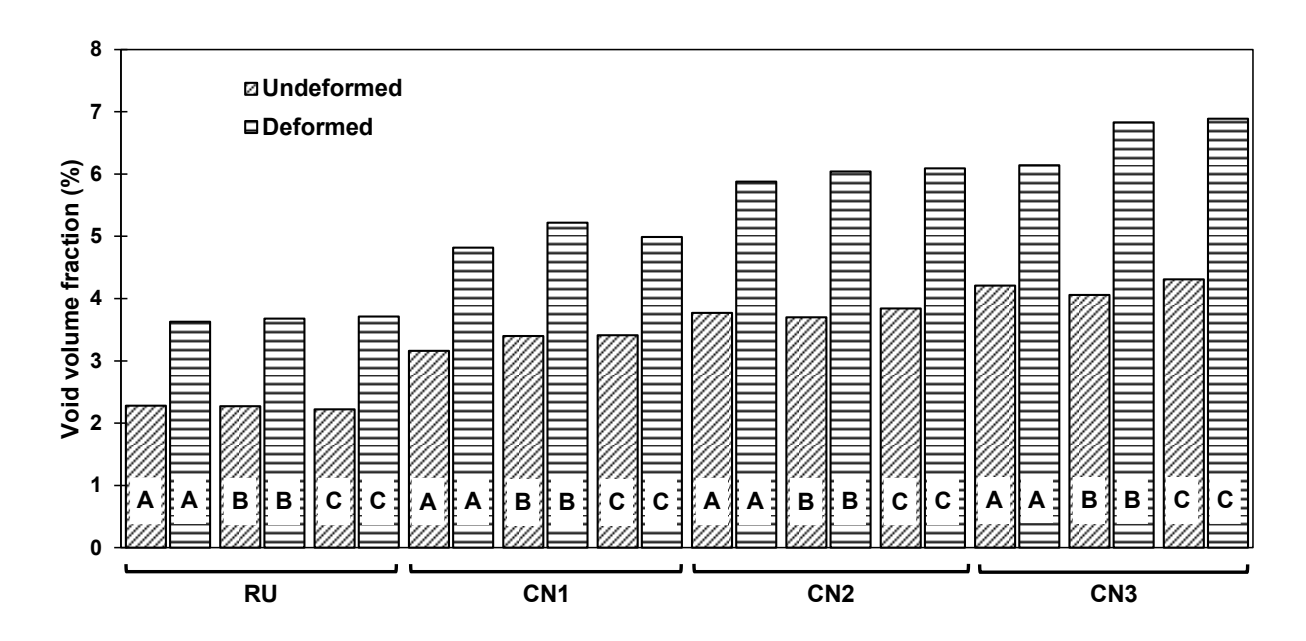


Figure 20. Comparison of the local void volume fraction in undeformed and deformed test specimens.

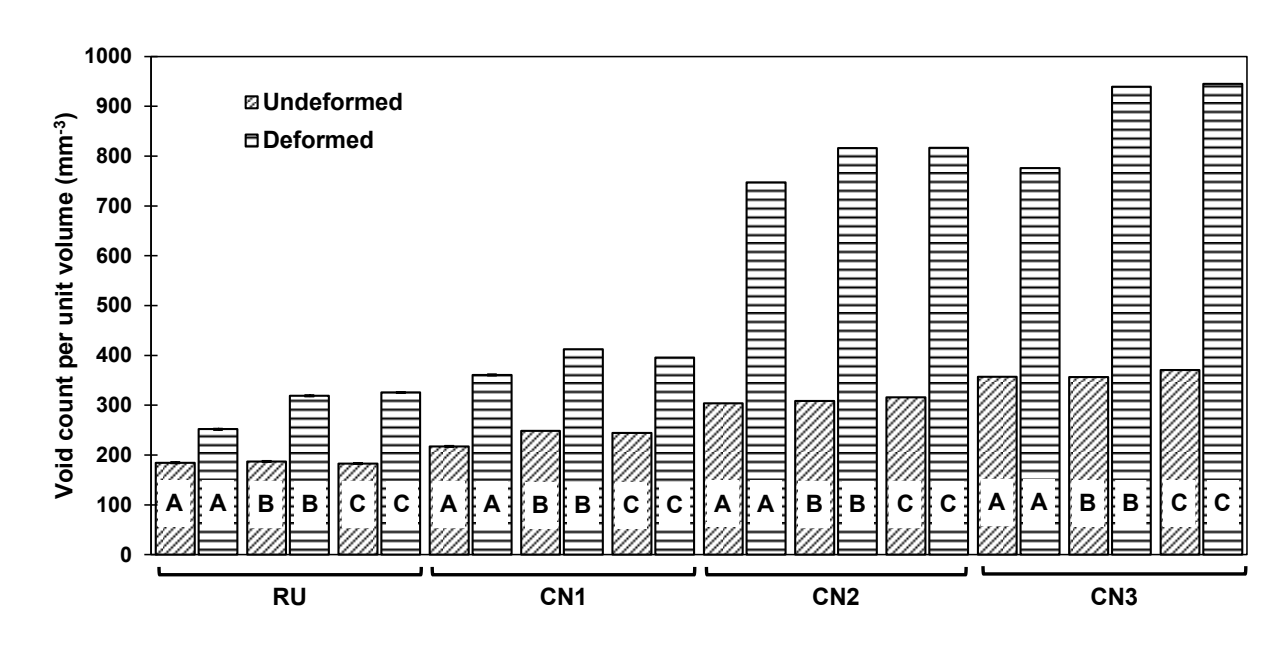


Figure 21. Comparison of the void count per unit volume in undeformed and deformed test specimens.

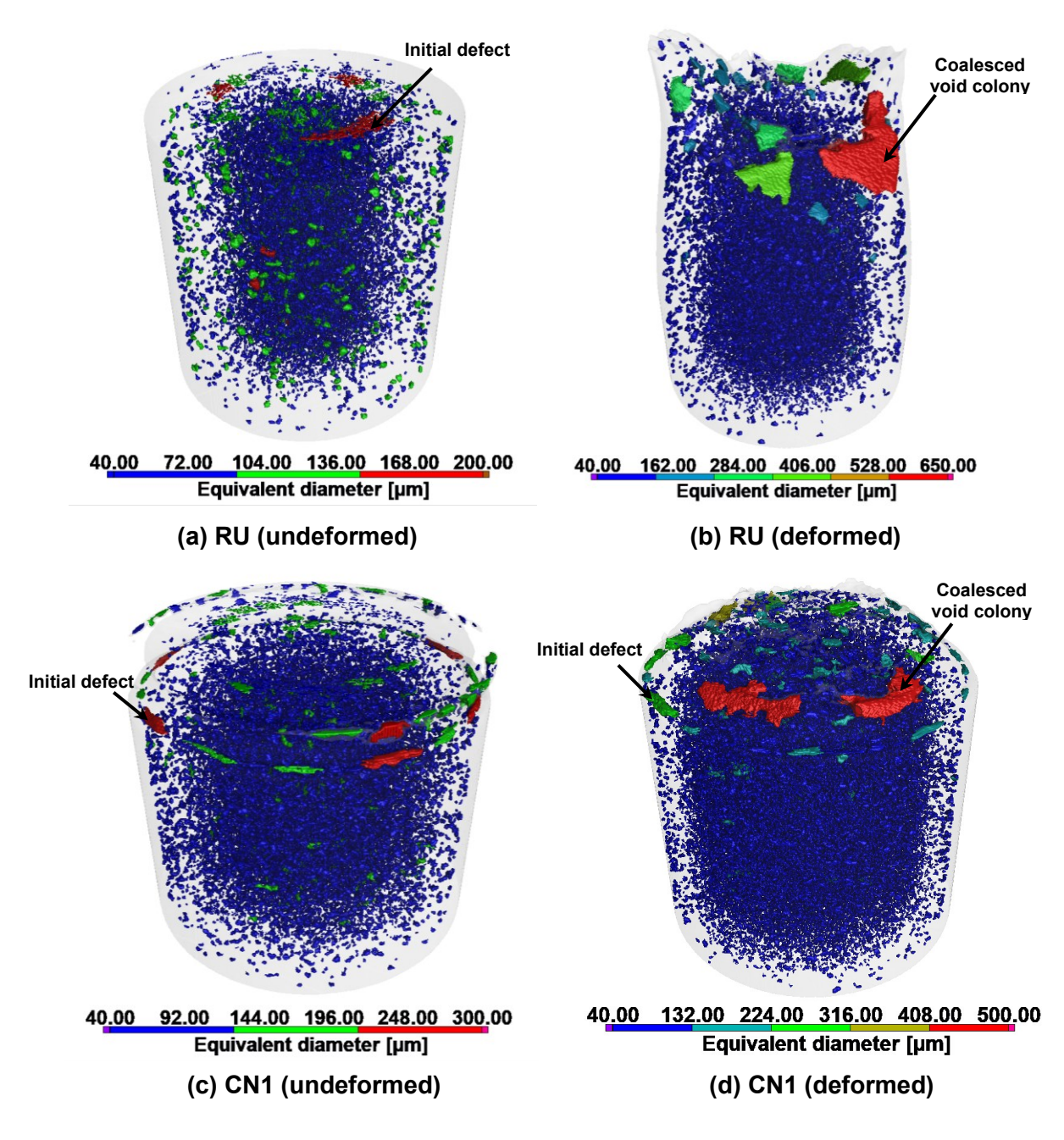


Figure 22. Defects in zone A before and after fracture for specimens (a,b) RU and (c,d) CN1.

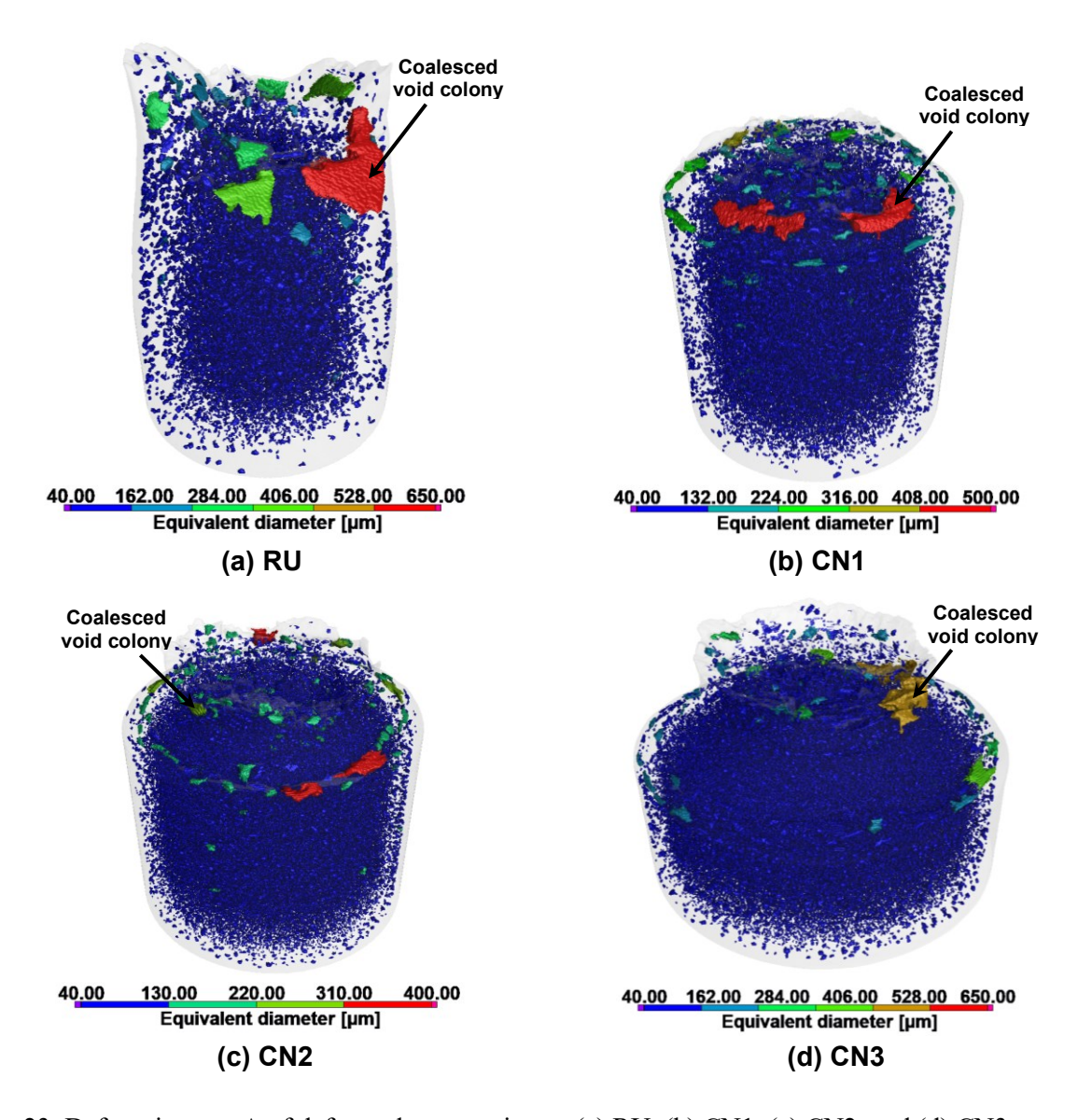


Figure 23. Defects in zone A of deformed test specimens (a) RU, (b) CN1, (c) CN2, and (d) CN3.